



HAL
open science

Catalytic application of ferrierite nanocrystals in vapour-phase dehydration of methanol to dimethyl ether

Enrico Catizzone, Stijn Van Daele, Micaela Bianco, Alessandro Di Michele, Alfredo Aloise, Massimo Migliori, Valentin Valtchev, Girolamo Giordano

► To cite this version:

Enrico Catizzone, Stijn Van Daele, Micaela Bianco, Alessandro Di Michele, Alfredo Aloise, et al.. Catalytic application of ferrierite nanocrystals in vapour-phase dehydration of methanol to dimethyl ether. *Applied Catalysis B: Environmental*, 2019, 243, pp.273-282. 10.1016/j.apcatb.2018.10.060 . hal-03039845

HAL Id: hal-03039845

<https://normandie-univ.hal.science/hal-03039845>

Submitted on 4 Dec 2020

HAL is a multi-disciplinary open access archive for the deposit and dissemination of scientific research documents, whether they are published or not. The documents may come from teaching and research institutions in France or abroad, or from public or private research centers.

L'archive ouverte pluridisciplinaire **HAL**, est destinée au dépôt et à la diffusion de documents scientifiques de niveau recherche, publiés ou non, émanant des établissements d'enseignement et de recherche français ou étrangers, des laboratoires publics ou privés.

1 **Catalytic application of ferrierite nanocrystals in vapour-phase**
2 **dehydration of methanol to dimethyl ether**

3 *Enrico Catizzone^{a*}, Stijn Van Daele^b, Micaela Bianco^a, Alessandro Di*
4 *Michele^c, Alfredo Aloise^a, Massimo Migliori^a, Valentin Valtchev^{b,d*},*
5 *Girolamo Giordano^a*

6 ^a Department of Environmental and Chemical Engineering, University of Calabria, Via
7 P. Bucci – I-87036 Rende (CS), Italy.

8 ^b Normandie Univ., ENSICAEN, UNICAEN, CNRS, Laboratoire Catalyse et
9 Spectrochimie, 14000 Caen, France.

10 ^c Department of Physics and Geology, University of Perugia, via Pascoli, 1 – 06123
11 Perugia, Italy.

12 ^d State Key Laboratory of Inorganic Synthesis and Preparative Chemistry, Jilin
13 University, Changchun 130012, China.

14
15 *Corresponding authors:

16 E-mail addresses: valentin.valtchev@ensicaen.fr (V. Valtchev) ORCID: 0000-0002-
17 2341-6397; enrico.catizzone@unical.it (E. Catizzone) ORCID: 0000-0002-3962-9493.

18
19 Authors' contributions are detailed below:

20 Enrico Catizzone: manuscript preparation; XRD and porosimetric analysis, TG/DTA;
21 manager of experimental part.

22 Stijn van Daele: manuscript preparation and revision; characterization of materials by
23 FT-IR analysis.

24 Massimo Migliori: manuscript preparation and revision; manager of experimental part.

25 Micaela Bianco: synthesis of materials and catalytic tests.

26 Alessandro Di Michele: characterization of exhausted catalysts.

27 Alfredo Aloise: Chemical and Physical analysis.

28 Valentin Valtchev: Research plan discussion and revision of the manuscript.

29 Girolamo Giordano: revision of the manuscript; manager of the research project.

30

31 **ABSTRACT**

32 *The FER-type zeolite was found to be a reliable catalyst for DME synthesis via both*
33 *direct CO₂ hydrogenation or gas phase methanol dehydration. In this work, the effect of*
34 *the crystal size of FER-type zeolites on the catalytic behavior during methanol-to-DME*
35 *conversion is studied. A series of FER-type crystals ranging from 0.1 μm to 10 μm in*
36 *size were synthesized and their physicochemical properties (e.g. crystal morphology,*
37 *acidity, textural characteristics) analyzed. The catalytic performance of FER-type*
38 *catalysts was studied in a wide range of reaction temperatures (120-280 °C). The set*
39 *experimental data show that the catalytic effectiveness of FER-type catalysts in terms of*
40 *methanol conversion, DME selectivity and coke resistance, can strongly be improved by*
41 *reducing the zeolite crystal size.*

42

43 **Keywords:** Ferrierite; Crystal morphology; Brønsted-Lewis acidity; Methanol
44 conversion; DME; Coke deposition.

45

46 **1. INTRODUCTION**

47 Zeolites are crystalline microporous aluminosilicates whose catalytic properties are
48 largely explored for decades. The ever-growing success of zeolites as industrial
49 catalysts is mainly resulting from their unique molecular shape-selectivity, owing to a
50 well-defined regular microporous structure, combined with tunable active sites.
51 Generally, both Brønsted and Lewis type acid sites are simultaneously present in a
52 zeolite and their concentration, distribution, strength and location affect the overall
53 activity, product selectivity and deactivation of the catalyst [1]. Unfortunately, the
54 exceptional shape selectivity of zeolites is coupled with severe intracrystalline mass
55 transfer limitations due to comparable size of the diffusing molecules and the zeolite
56 channels. The interaction between diffusing molecules and channel walls, known as
57 configurational diffusion, hinders the reaction rate and reduces the catalyst efficiency.
58 In order to overcome this problem, one of the strategies to be adopted in order to reduce
59 mass transfer limitation is to synthesise zeolites with a secondary pore system of larger
60 channels [2]. In this class of materials, known as hierarchical or mesoporous zeolites,
61 intrinsic micropores are connected with a mesoporous channel net, promoting the
62 diffusion to/from the active sites. During the last decade, several methods have been
63 developed for hierarchical zeolites preparation, using bottom-up or top-down
64 approaches [2-4]. Depending on the adopted procedure, pore architecture, position and
65 topology of mesopores of zeolites can be varied and thus their catalytic performances
66 [5, 6].

67 The reduction of the crystal size to nanometric scale is another option largely explored
68 in order to reduce the diffusion path length and thus to increase catalyst effectiveness

69 [8-9]. Yang *et al.* [10] showed that the crystal size strongly affects both product
70 distribution and catalyst deactivation, during methanol (MeOH) conversion to olefins
71 over SAPO-34 catalysts (CHA-type structure). Namely, the utilization of nano-sized
72 SAPO-34 remarkably enhanced the olefins yield and catalyst life time and the positive
73 effect of nano-zeolites in methanol-to-olefin conversion was also reported by other
74 authors [11-15]. The superiority of nano-sized zeolite in catalysis has also been
75 demonstrated for other zeolite-catalysed reactions such as *n*-hexane cracking [16],
76 hydrocracking of heavy vacuum gas oil [17, 18], Fischer-Tropsch process [19], alkane
77 and xylene isomerization [20, 21], biomass pyrolysis [22], ethanol to propylene [23]
78 and others [24].

79 Nano-sized zeolite crystals can be obtained via a careful optimization of the synthesis
80 gel composition and crystallization conditions, as summarized by Mintova *et al.* [25,
81 26] and Di Renzo [27]. One key factor is the ability to induce simultaneous nucleation
82 events, producing a zeolite with narrow particle size distribution. Such conditions were
83 achieved for several industrial relevant zeolites by fine control of the reaction
84 parameters (e.g. gel composition, alkalinity, dilution, temperature, gel aging, etc.) [7,
85 25-32].

86 Recently, the crystallization of zeolites in the presence of a surfactant was reported as
87 an unconventional method to prepare nano-sized MFI and MOR crystals [33-35].
88 Different surfactants, anionic, cationic or non-ionic molecule, can be employed.

89 SLS was proposed as an emulsifier to obtain highly crystalline nano-sized FER crystals
90 in the range 200-400 nm when piperidine is used as a structure directing agent. CTABr
91 or Span 60 will lead to the formation of an amorphous phase and 1-3 μm large ferrierite
92 crystals, respectively [36].

93 Recent works showed that the FER-type zeolite is promising acid catalyst to produce
94 dimethyl ether (DME) via both methanol dehydration [37-39] and one-pot CO₂
95 hydrogenation [40-42]. DME has a bright future ahead as a reliable alternative fuel for
96 diesel engines due to its high cetane number and soot-free emissions [43]. Moreover,
97 DME can also be an intermediate in the olefins and fine chemicals production, and it is
98 considered as a reliable energetic vector to introduce renewable energy in the chemical
99 industry [44, 45], since it can be produced from biomass or CO₂.

100 Compared with other zeolite catalysts (e.g. beta, MFI, MOR, MTW, EU-1), the
101 ferrierite shows a higher DME selectivity and resistance to deactivation by coke
102 deposition [38, 42]. The effect of acidity of the FER-type zeolite on methanol
103 dehydration to DME reaction was also investigated revealing that a higher Lewis acid
104 concentration will increase the catalyst effectiveness [46]. The beneficial use of nano-
105 sized zeolites in methanol dehydration to dimethyl ether reaction was recently
106 investigated by Rownaghi *et al.* [47] using ZSM-5 zeolites. The authors showed that by
107 reducing the crystal size from 1.2 μm to 0.12 μm, both the DME selectivity and the
108 MeOH conversion improved significantly.

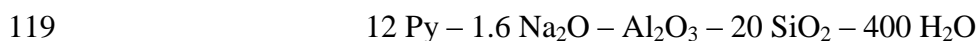
109 According to that, the aim of this study is to investigate the behaviour of nanosized
110 FER-zeolites in DME synthesis. The crystals size was varied from nano- to micron-
111 sized dimension and the impact of crystals size on the number and distribution of active
112 sites was studied in vapour phase methanol dehydration.

113

114 **2. EXPERIMENTAL**

115 *2.1 Samples preparation*

116 All FER-type zeolite samples were prepared by using pyrrolidine (Py, Aldrich) as
117 structure directing agent (SDA) adopting the synthesis procedure described elsewhere
118 [29] and using a gel with the following molar composition:



120 The used chemicals were: Colloidal silica Ludox AS-40 (SiO_2 , 40 wt% suspension in
121 water, Aldrich), sodium aluminate (NaAlO_2 , Aldrich), sodium hydroxide (Aldrich) and
122 distilled water.

123 All the syntheses were carried out in 60 ml PTFE-lined stainless steel autoclaves using a
124 tumbling oven (tumbling speed = 20 rpm). The crystallization of micron-sized FER-
125 type zeolite (named M-FER) was carried out at 180 °C for 120 h. With the aim to
126 reduce the crystal size, sodium lauryl sulfate (SLS, Aldrich) was used as a surfactant in
127 the sampled labelled as NP-FER. A SLS/ Al_2O_3 molar ratio equals to 0.3 was used and
128 crystallization was carried out at 180 °C for 75 h.

129 The effect of seeds was also evaluated by adding 3 wt. % seeds (H-form NP-FER) with
130 respect to silica in the above reported synthesis gel. Crystallization of this system was
131 performed at 160 °C for 60 h and before synthesis, the gel was aged at 80 °C for 48 h
132 under stirring condition (stirring rate: 500 rpm). The solid synthesized following this
133 from this procedure is reported as NC-FER.

134 As standard procedure, after synthesis, the solid was recovered by suction filtration and
135 washed several times with distilled water. Organic SDA was removed by calcination in
136 air at 550 °C for 8 h. After this treatment, the H-form of the synthesized zeolites was
137 prepared by an ion-exchange with NH_4Cl solution [37], followed by calcination in air
138 (550 °C for 8 h).

139

140 2.2 Physicochemical characterization

141 Powered X-ray diffraction patterns of synthesised samples were obtained with APD
142 2000 Pro GNR instrument (Cu K α radiation, $\lambda=1.5406$, 40 kV, 30 mA, 5-50° 2 θ range,
143 scanning step 0.2°·s⁻¹). The crystal size and shape were studied using a scanning
144 electron microscope (FEI model Inspect). Nitrogen adsorption/desorption isotherms
145 were carry out on H-form samples at 77 K with a Micromeritics ASAP 2020. The
146 specific surface area was calculated using the BET equation, whilst the micropore
147 volume and external surface were estimated by the *t*-plot method. Thermogravimetric
148 analysis (TG/DTA) was carried out in air on a DTG-60 Shimadzu instrument in the
149 range 25 °C - 850 °C (heating rate: 5 °C·min⁻¹). The chemical composition of the
150 samples was determined via atomic absorption spectroscopy (GBC 932). ²⁷Al-NMR
151 spectra of H-form samples were acquired on a Bruker Advance 500 MHz spectrometer
152 [48].

153 The *in-situ* FT-IR technique was used to study the surface acidity of the samples. FTIR
154 measurements were carried out on a Nicolet Magna 550-FTIR spectrometer at 4 cm⁻¹
155 optical resolution with a DTGS detector. Samples to be analysed were pressed as self-
156 supported wafers (diameter 13 mm, 18 mg). Before the spectrum acquisition at room
157 temperature, each sample was pre-treated in the IR cell connected to the vacuum line at
158 393 K (1 K/min) for 4 h and at 723 K (1 K/min) for 5 h under 10⁻⁶ torr. Deuterated
159 acetonitrile (CD₃CN) was used as a probe to estimate total acidity and Brønsted/Lewis
160 distribution as this base molecule is able to diffuse in both 8- and 10-membered rings of
161 FER structure. 2,6-dimethyl pyridine and *tert*-butyl nitrile were used as probe molecules
162 to estimate the number of Brønsted and Lewis acid sites located on the external crystal

163 surface. Probe molecules were adsorbed at room temperature (295 K) with a saturation
164 pressure of 0.5 torr.

165 *2.3 Catalytic tests*

166 Vapor-phase methanol dehydration reaction was carried out in a lab-scale apparatus,
167 using a quartz tubular reactor [49]. A mixture of methanol/nitrogen (methanol content
168 0.06 mol/mol) was fed to the reactor containing 70 mg of catalyst (pellets form 300-500
169 μm) with a total flow rate of 60 $\text{Nml}\cdot\text{min}^{-1}$. Catalytic tests were carried out in the 120-
170 280 $^{\circ}\text{C}$ range under atmospheric pressure. Stability tests were performed at 280 $^{\circ}\text{C}$ for a
171 duration up to 60 h. Reactor out-stream composition was analyzed by an on-line gas-
172 chromatograph equipped with flame ionization detector [49].

173 *2.4 Coke analysis*

174 The amount of carbonaceous solid (named coke) deposited during time-on-stream tests
175 at 280 $^{\circ}\text{C}$ was determined via thermogravimetric analysis of exhausted samples [37].
176 The composition of coke was measured via GC-MS analysis following a
177 dissolving/extracting procedure [38]. The morphology and distribution of coke on
178 zeolite surface was also investigated by Field Emission Gun Electron Scanning
179 Microscopy LEO 1525 ZIESS, after metallization with Cr and elemental composition
180 was determined using a Bruker Quantax EDS.

181

182 **3. RESULTS AND DISCUSSION**

183 *3.1 Physicochemical properties of investigated samples*

184 XRD analysis showed that all samples are highly crystalline FER-type materials, neither
185 other phases nor amorphous material was identified (Figure 1). SEM images of M-FER,

186 NP-FER and NC-FER are shown in Figure 2(A)-(C), respectively. M-FER shows
187 stacked plate-like crystals with a well-developed $\{1\ 0\ 0\}$ face with following
188 dimensions: length 8-12 μm , length/width ratio around 2 μm and thickness 0.1 μm
189 (Figure 2A). The use of SLS surfactant resulted in the formation of non-stacked plate-
190 like crystals with size ranging between 300 and 500 nm (Figure 2B). The addition of
191 seeds allowed to decrease the crystal size to about 100 nm (Figure 2C). Chemical
192 analysis data reported in Table 1 show that the samples exhibit a similar bulk
193 aluminium content (AC), but a higher aluminium content on the surface (AS) was
194 found, with major evidence for smaller crystals. The analysis of the local structure by
195 ^{27}Al MAS NMR is presented in Figure S.1 (Supplementary Information), revealing that
196 both, tetrahedral and octahedral aluminium species, are present in the investigated
197 samples, with a chemical shift of about 54 ppm and 0 ppm, respectively. The relative
198 concentration of octahedral aluminium increases as the crystal size decreases from ca.
199 14% of the largest crystals to ca. 21% for the smallest ones (Table 1). The higher AS in
200 the nanocrystals is obviously related to the presence of extra-framework aluminium on
201 their outer surface.

202 The N_2 adsorption/desorption isotherms at 77 K presented in Figure 3 reveal some
203 differences in the porosity and the texture of the investigated samples. M-FER exhibits
204 a type-I isotherm, where a second uptake is observed at 0.7-0.8 relative pressure with
205 hysteresis. in the later is a consequence of stacking of platelets of about 100 nm
206 thickness [50, 51]. NP-FER exhibits a less evident hysteresis loop probably due to
207 limited agglomeration between the particles [52]. On the contrary, NC-FER exhibit a
208 type-H4 hysteresis loop at lower relative pressure (starting from about 0.4) typical of
209 agglomerates of particles forming mesopores with uniform size and shape [51-54]. As

210 reported in Table 1 both BET surface area and micropore volume are typical of highly
211 crystalline FER-type materials [29]. The differences in micropore volume could be
212 related to the presence of extra-framework aluminium species inside the pores, since
213 samples with a higher concentration of extra-framework aluminium species exhibit
214 lower micropore volume. The analysis of the local structure of aluminium by ^{27}Al MAS
215 NMR is presented in Figure S.1 (Supplementary Information), revealing that both,
216 tetrahedral and octahedral aluminium species, are present in the investigated samples,
217 with a chemical shift of about 54 ppm and 0 ppm, respectively. The relative
218 concentration of octahedral aluminium increases as the crystal size decreases from ca.
219 14% of the largest crystals to ca. 21% for the smallest ones (Table 1).

220 Figure 4(A) shows the FT-IR spectra of investigated FER-type samples prior to the
221 adsorption of the probe molecule. The sharp band at 3746 cm^{-1} is associated with
222 terminal silanol groups located on the external surface. The shoulder at $3720\text{-}3730\text{ cm}^{-1}$
223 originates from silanols located inside the pores. The band at 3600 cm^{-1} is characteristic
224 of bridging $\text{Si}(\text{OH})\text{Al}$ Brønsted sites. The broad shoulder around 3650 cm^{-1} is typically
225 related to highly distorted or extra-framework aluminium species that can act as Lewis
226 acid sites [55-59]. Spectra reported in Figure 4 reveal that all the samples show similar
227 bands in the $3720\text{-}3746\text{ cm}^{-1}$ region, suggesting similar concentration and location of
228 silanol groups. On the contrary, FT-IR spectra differ in the $3600\text{-}3680\text{ cm}^{-1}$ region: the
229 band height at 3600 cm^{-1} follows the order $\text{M-FER} > \text{NP-FER} > \text{NC-FER}$ suggesting that
230 M-FER possess a higher concentration of bridging $\text{Si}(\text{OH})\text{Al}$ Brønsted sites than the
231 other samples. NC-FER contains a more pronounced band at $3630\text{-}3680\text{ cm}^{-1}$ region
232 showing a higher concentration of extra-framework aluminium species for nanosized
233 sample, in agreement with the ^{27}Al MAS NMR data.

234 In order to better discriminate between Lewis and Brønsted acid sites, in the 3600-3680
235 cm^{-1} region the bands entirely disappear after the adsorption of CD_3CN , indicating that
236 the acid sites of investigated samples are fully saturated (Figure 4(B)). A small number
237 of terminal silanols are still present after CD_3CN adsorption, confirming the low-acidic
238 character of these groups, whilst internal silanols (bands at around 3725 cm^{-1}) totally
239 disappear.

240 Spectra analysis suggests that d_3 -acetonitrile exhibits at least five stretching modes of
241 $\nu(\text{C}\equiv\text{N})$ in the region $2220\text{-}2360 \text{ cm}^{-1}$ as reported in Figure S.2. IR band at about 230
242 cm^{-1} is ascribed to coordinatively bonded CD_3CN on electron acceptor aluminium sites
243 that act as Lewis centres whereas the band at $2296\text{-}2298 \text{ cm}^{-1}$ derives from coordination
244 of probe molecule with bridging OH groups that act as Brønsted acid sites. The
245 presence of a $\nu(\text{C}\equiv\text{N})$ stretching band at $2275\text{-}2280 \text{ cm}^{-1}$ is associated to the interaction
246 of CD_3CN with zeolite defects (i.e., silanols) whereas the presence of physisorbed and
247 liquid phase CD_3CN is characterized by the bands at 2265 cm^{-1} and 2250 cm^{-1} ,
248 respectively [60, 61]. The number of bridging Brønsted sites was calculated from the
249 area of the band observed at 2296 cm^{-1} by adopting an extinction coefficient of 2.05
250 $\text{cm}/\mu\text{mol}$, whilst the number of Lewis acid sites was calculated from the area of the
251 band centered at 2322 cm^{-1} by adopting an extinction factor of $3.6 \text{ cm}/\mu\text{mol}$ [60].

252 In order to probe the external surface of ferrierite crystals two bulky molecules, 2,6-
253 dimethyl pyridine (lutidine) and tert-butyl nitrile (pivalonitrile), were employed. The
254 difference spectra after saturation with lutidine are presented in Figure 5(A). Besides the
255 bands characteristic of lutidine, a negative signal due to the consumption of silanols is
256 observed at 3747 cm^{-1} . This result shows that the majority of silanols are situated at the
257 external surface of ferrierite, which is in agreement with the data reported by van Donk

258 *et al.* [62]. The relative magnitude of the signal at 3600 cm^{-1} , representing the
259 consumption of Brønsted acid sites, points out that only a small percentage of the total
260 Brønsted acid sites is consumed by lutidine. By analysing the spectra in the $1700\text{-}1500$
261 cm^{-1} range both bands specific for lutidine:Lewis at $1580\text{-}1603\text{ cm}^{-1}$ and
262 lutidine:Brønsted at $1630\text{-}1650\text{ cm}^{-1}$ appear. As reported elsewhere [63, 64] lutidine is
263 strongly adsorbed on Brønsted even after outgassing at high temperature whilst readily
264 desorbs from the Lewis sites because of limited interaction by steric hindrance. For this
265 reason, lutidine is considered a suitable probe molecule to estimate Brønsted sites [64,
266 65]. The Brønsted acid sites on the external surface were estimated by the band at 1630-
267 1650 cm^{-1} using the molar extinction coefficient reported by Onfroy *et al.* [66]. In order
268 to quantify external Lewis acidity probing with *tert*-butylnitrile was employed. On the
269 other hand, due to overlapping signals, quantification of the Brønsted acidity by *tert*-
270 butylnitrile molecule is hindered. Based on the literature data both, the molar extinction
271 coefficient and the identification of different bands, was performed [67, 68]. As
272 reported in Figure 5(B), the coordination between the probe molecule on a Lewis site is
273 found at 2305 cm^{-1} . Although a high percentage of Lewis acidity is observed in all three
274 samples, no surface enrichment is detected.

275 The quantification of acid sites resulted from FT-IR analysis is summarized in Table 2.
276 NP-FER sample shows the highest Lewis acid sites concentration followed by NC-FER
277 and M-FER. On the contrary, the highest bridging Brønsted acid sites concentration is
278 measured for M-FER followed by NP-FER and NC-FER. Note that the investigated
279 samples possess a similar aluminium content. Therefore, the set of data points out that
280 the smaller crystals contain less Brønsted sites than larger ones. We relate this result
281 with the synthesis conditions used to obtain nanocrystals that might cause a lower

282 aluminium incorporation [69]. Although NC-FER exhibits the highest aluminium
283 content on the external surface, the lower amount of external acid sites was found on
284 this sample, indicating that not all the external aluminium species possess acidity
285 properties [69].

286 For all the samples, less than 2% of total acid sites are located on the external surface of
287 zeolite crystals suggesting that the majority of acid sites, either Brønsted- or Lewis-
288 type, are mainly located in the pore volume. The latter result permits to assume that the
289 effect of the external surface acidity is negligible in comparison with the internal acidity
290 on catalytic behaviour of investigated zeolites.

291

292 *3.3 The effect of crystal size on catalytic activity*

293 The methanol conversion is reported in Figure 6 in the reaction temperature range
294 120°C - 280°C. The following activity order NP-FER>NC-FER>M-FER can be
295 observed up to 220 °C whilst all catalysts exhibit a similar conversion, close to the
296 equilibrium thermodynamic value, at high temperatures. Since the observed differences
297 in catalytic activity can be related to both acidity and crystal size, a turnover frequency
298 (TOF) analysis was employed to shed more light in the catalytic reaction. Both intrinsic
299 reaction rate and an accurate counting of active sites are necessary in order to estimate a
300 TOF value. It is well-known that only an apparent reaction rate can be calculated when
301 zeolites are used as catalyst due to severe intracrystalline mass transfer limitation;
302 furthermore, both Brønsted and Lewis acid sites catalyse dehydration of methanol to
303 DME, even if Lewis acid sites show a higher activity [46, 70]. Therefore, in this work,
304 an apparent turnover frequency (TOF_{app}) value is calculated by considering the

305 observable methanol conversion rate and both Brønsted and Lewis acid sites number
306 calculated from FT-IR analysis. Silanols sites were not included since they are not
307 active towards such reaction under the investigated conditions. TOF_{app} is calculated by
308 the following equation:

$$309 \quad TOF_{app} = \frac{n_{n_{MeOH}}^0 \cdot X_{MeOH}}{B + L}$$

310 with $n_{n_{MeOH}}^0$ the inlet methanol flow rate (e.g. expressed in $\mu\text{mol/h}$), X_{MeOH} the methanol
311 conversion grade (dimensionless) and B and L are Brønsted and Lewis acid sites
312 number, respectively. The apparent TOF analysis was performed with conversion data
313 at 180°C [38] and the estimated values are reported in Table 3. The obtain values show a
314 positive effect of reducing crystal size on the efficiency of the catalyst in terms of
315 apparent turnover rate since TOF_{app} increases from 45 h^{-1} to 65 h^{-1} by decreasing the
316 crystal size from micro- to nano-metric scale. A recent work reports that Lewis acid
317 sites exhibit higher activity than Brønsted acid sites during methanol to DME reaction
318 leading to higher TOF value for FER-type zeolites with higher Lewis acid sites
319 concentration [46]. The results obtained in this work report that, although NC-FER
320 possesses a LAS concentration much lower than NP-FER, it exhibits a higher apparent
321 TOF indicating that the control of mass transfer limitation in zeolites plays a crucial role
322 in Methanol-to-DME reaction.

323 For reaction temperatures up to 220°C , DME was detected in the reactor out-stream, in
324 agreement with previous studies [37-39]. At 240°C , traces of hydrocarbons, mainly
325 methane, ethylene and propylene are formed, causing a DME selectivity drop; which is
326 more critical for larger crystals while no by-products were detected when NC-FER was
327 tested (see Table 3).

328 By increasing the reaction temperature to 280 °C, DME selectivity decreases to 95%
329 and 90% for NP-FER and M-FER, respectively. The DME selectivity is about 99% for
330 NC-FER. For both, NP-FER and M-FER, by-products were quantified from GC
331 analysis whilst similar analysis was not possible for NC-FER because of too low
332 signals. Methane, ethene and propene were mainly formed as by-products. In particular,
333 the distribution of by-products loop is reported in Table 3. The results clearly show that
334 the ethene fraction is similar in M-FER and NP-FER samples whilst the yield of
335 methane was higher on the NP-FER sample, probably related to its higher Lewis acid
336 sites concentration [46].

337 It is known that the formation of hydrocarbons from methanol, involves a complex
338 mechanism (such as hydrocarbon pool in the case of olefins) where methanol might be
339 dehydrated to DME and then both DME and methanol are converted to hydrocarbons
340 [71-75]. The obtained selectivity results suggest that in case of nano-sized crystals it is
341 possible to reduce the residence time inside the crystal and, as a consequence, formed
342 DME is able to effectively diffuse outside the crystal reducing the occurrence of
343 consecutive reactions [13, 75]. On the contrary, on large crystals (e.g. M-FER), more
344 side reactions can occur. Time-On-Stream tests carried out at 280 °C showed that all
345 catalysts keep a nearly constant methanol conversion grade for 60 h (Figure S.3,
346 Supporting Information). Smaller crystal (NP-FER and NC-FER) showed stable DME
347 selectivity up to 60 h. The selectivity of micron-sized crystals (M-FER) increased from
348 0.90 to 0.98 after 60 h.

349

350 *3.4 Coke analysis*

351 The amount of coke deposited on the investigated catalysts during methanol
352 dehydration at 280 °C monitored via Thermogravimetric/Differential Thermal Analysis
353 (TG/DTA) is presented in Figure 7. It clearly appears how the coke deposition is
354 favourably affected by the increase in crystal size: the measured amount of deposited
355 coke is 75 mg_{coke}/g_{cat}, 69 mg_{coke}/g_{cat} and 46 mg_{coke}/g_{cat} for M-FER, NP-FER and NC-
356 FER, respectively, after 60 h of Time-on-Stream.

357 In order to obtain quantitative information on the coke formation rate, the experimental
358 data was fitted to a first order model [37]:

$$359 \quad C = C_{\infty} \cdot \left(1 - e^{-t/\tau}\right) \quad (1)$$

360 where C is the specific coke amount (mg_{coke}/g_{cat}), C_{∞} the plateau value and τ the
361 characteristic time (h). From this equation, the initial coke deposition rate r_0
362 (mg_{coke}/(g_{cat}·h)) can be estimated as:

$$363 \quad r_0 = \left. \frac{dC}{dt} \right|_{t=0} = \frac{C_{\infty}}{\tau} \quad (2)$$

364 The experimental data were fitted via a nonlinear regression by using a commercial
365 software (Curve Expert Professional 2.0) and the model parameters values are
366 summarized in Table 4. The calculated kinetic parameters suggest that the crystal size
367 strongly affects the kinetics of coke formation, in terms of either carbon amount or
368 deposition rate. In fact, by decreasing the crystal size both C_{∞} and r_0 are reduced as a
369 consequence of the utilization of nanosized zeolite in methanol-to-DME dehydration.

370 In order to establish the composition of the deposited carbon, a coke extraction
371 procedure was carried out following the method developed by Guisnet and Magnoux
372 [76]. No insoluble carbon particles were observed, suggesting that all the carbonaceous

373 deposits can be referred to “soluble coke” which can be analyzed via GC-MS technique.
374 Figure 8 reports the GC-MS spectra for the extracted carbonaceous deposits for the
375 samples after 5 h, 15 h and 60 h of reaction. This analysis revealed that no
376 polyaromatics were detected and the coke-forming compounds are poly-substituted
377 benzenes with a grade of substitution depending on reaction time and crystal size. Over
378 the micron-sized ferrierite crystal (M-FER), the coke is mainly composed from di-
379 methyl benzene (Di-MB) and tetra-methyl benzene (Tetra-MB) with traces of hexa-
380 methyl benzene (Hexa-MB). The same identity of coke molecules are detected for NC-
381 FER, whereas NP-FER only forms Tetra-MB.

382 Di- and Tetra-MB can be accommodated in ferrierite cages, whilst bulkier molecules,
383 such as Hexa-MB, are most probably formed on the external surface [77, 78]. The
384 formation of Hexa-MB on the NC-FER sample might be related to the crystal
385 morphology of this sample. The clustering of nano-crystals may induce inter-crystalline
386 mass transfer limitations, higher retention time, and thus increase the probability of a
387 transformation of precursors molecules into Hexa-MB. Hexa-MB is also detected in M-
388 FER, where stacking along the pinacoidal plane is largely observed. In contrast the
389 small single crystals of the NP-FER sample ensure a fast release of coke precursors
390 from the crystal surface. Consequently no Hexa-MB is observed. As the reaction time
391 increases, Tetra-MB becomes the main observed carbonaceous species for NP-FER,
392 while larger M-FER and NP-FER crystals contain tetra-MB and di-MB molecules.

393 Figure 9 presents the DTA profiles for the series of catalysts after 5 h, 15 h and 60 h
394 reaction at 240 °C. The exothermic peaks are related to the combustion of carbonaceous
395 species, revealing that this effect occurs at different temperatures and depends on both,
396 the reaction time and crystal size.

397 This is in agreement with the earlier discussed GC-MS analysis as, when Hexa-MB is
398 present, which is the case after 5 h of reaction for NC-FER and M-FER samples, a
399 combustion peak is present at a relatively low temperature (i.e. 285°C and 274 °C,
400 respectively). This peak can then be associated with the combustion of Hexa-MB
401 located on the external surface of the crystals. In fact, when Hexa-MB is absent, the
402 combustion phenomena take place at a higher temperature and it can be attributed to the
403 thermal degradation of Di- or Tetra-MB molecules trapped within the micropores. On
404 the other hand, if Tetra-MB is the only present specie, as in the case of NP-FER after 15
405 h reaction, the exothermic peaks appear at ca. 344 °C, 435°C and 590 °C suggesting
406 different locations and force of interaction between the molecule and FER framework.
407 On the basis of DTA profiles, the carbon deposit can be classified as low temperature
408 coke (LTC) and high temperature coke (HTC) associated to carbon deposit burning
409 below or above 500 °C, respectively. According to this classification, it is possible to
410 calculate the amount of LTC and HTC from thermogravimetric analysis and assess the
411 effect of reaction time on HTC/LTC. Figure 10 shows that HTC/LTC ratio increases as
412 a function of reaction time in the following order M-FER>NP-FER>NC-FER. The data
413 unambiguously show that the decrease of crystal size leads to reduction of HTC.
414 Consequently, the deposited carbon can be eliminated by using milder regeneration
415 conditions. In order to gain a better understanding of the location of the carbonaceous
416 species, SEM-EDX analysis was performed (Figure 11). The EDX mapping clearly
417 reveals that the external coke is homogenously distributed on NC-FER crystals while
418 large carbonaceous agglomerates form on zeolites with larger crystals. This data also
419 confirm that the zeolite crystal size/morphology play a fundamental role in coke
420 deposition in terms of amount, composition and distribution.

421

422 **4. CONCLUSIONS**

423 The vapour-phase dehydration of methanol to dimethyl ether on FER-type zeolite
424 crystals was studied. The set of experimental data show that the decrease of crystal size
425 from 5-10 μm to 100 nm leads to an increase of methanol apparent turnover frequency
426 due to reduced intracrystalline mass transfer limitation and improved acid sites
427 accessibility. At 240 $^{\circ}\text{C}$ DME selectivity increases from 0.96 to 0.98 by reducing the
428 crystal size from 5-10 μm to 300-500 nm whereas no by-products were detected for
429 smaller nano crystals., By-products distribution analysis indicated that methane is
430 preferably formed foron catalysts with higher Lewis sites concentration. The thorough
431 assessment of the carbon deposition process revealed that: (i) The coke consists of
432 polymethyl benzene (PMB) molecules whose composition depends on both the zeolite
433 crystal morphology and the reaction time. The formation of Hexa-MB is observed
434 during the first 5 h for samples with intracrystalline voids, while only Di-MB and Tetra-
435 MB are observed for longer reaction time. The relative Di-MB/Tetra-MB ratio
436 decreases with the reduction of crystal size. Furthermore, (ii) the coke deposition can be
437 reduced and slowed down in rate by using zeolites with smaller crystals and (iii) the
438 regeneration of nano-sized zeolite catalysts can be performed at a lower temperature. As
439 a general conclusion, this work showed that the nano-sized FER-type crystals are a
440 much more efficient catalyst in methanol dehydration to DME with respect to their
441 micron-sized counterparts.

442

443 **ACKNOWLEDGMENTS**

444 The authors gratefully acknowledge Dr. Pietro Argurio (University of Calabria) for
445 chemical analysis via atomic absorption spectroscopy and Dr. Paola Lanzafame and Dr.
446 Georgia Papanikolaou (University of Messina) for chemical analysis via EDX.

447

448 **REFERENCES**

449 [1] A. Corma, State of the art and future challenges of zeolites as catalysts. *J.*
450 *Catal.* 216 (2003) 298-312.

451 [2] J. Pérez-Ramírez, C. H. Christensen, K. Egeblad, C. H. Christensen, J. C.
452 Groen, Hierarchical zeolites: enhanced utilisation of microporous crystals
453 in catalysis by advances in materials design. *Chem. Soc. Rev.* 37 (2008)
454 2530-2542.

455 [3] D. Verboekend, J. Pérez-Ramírez, Design of hierarchical zeolite catalysts
456 by desilication. *Catal. Sci. Technol.* 1 (2011) 879-890.

457 [4] Z. Qin, L. Lakiss, J.-P. Gilson, K. Thomas, J.-M. Goupil, C. Fernandez, V.
458 Valtchev, Chemical equilibrium controlled etching of MFI-type zeolite
459 and its influence on zeolite structure, acidity, and catalytic activity. *Chem.*
460 *Mater.* 2013, 25, 2759-2766.

461 [5] M. Milina, S. Mitchell, P. Crivelli, D. Cooke, J. Pérez-Ramírez, Mesopore
462 quality determines the lifetime of hierarchically structured zeolite
463 catalysts, *Nature Comm.* (2014) 3922.

464 [6] Z. Qin, J.-P. Gilson, V. Valtchev, Mesoporous zeolites by fluoride etching
465 *Current Opinion in Chemical Engineering*, 2015, 8, 1-6

- 466 [7] M. Choi, K. Na, J. Kim, Y. Sakamoto, O. Teresaki, R. Ryoo, Stable single-
467 unit-cell nanosheets of zeolite MFI as active and long-lived catalysts.
468 Nature 461 (2009) 246-249.
- 469 [8] A. Corma, V. Fornes, S. B. Pergher, T. L. Maesen, J. Buglass,
470 Delaminated zeolite precursors as selective acidic catalysts. Nature 396
471 (1998) 353.
- 472 [9] V. Valtchev, L. Tosheva, Porous nanosized particles: preparation,
473 properties, and application. Chem. Review 113 (2013) 6734-6760.
- 474 [10] G. Yang, Y. Wei, S. Xu, J. Chen, J. Li, Z. Liu, J. Yu, R. Xu, Nanosize-
475 enhanced lifetime of SAPO-34 catalysts in methanol-to-olefin reactions. J.
476 Phys. Chem. C 117 (2013) 8214-8222.
- 477 [11] N. Nishiyama, M. Kawaguchi, Y. Hirota, D. Van Vu, Y. Egashira, K.
478 Ueyama, Size control of SAPO-34 crystals and their catalyst lifetime in
479 the methanol-to-olefin reaction. Appl. Catal. A: Gen. 362 (2009) 193-199.
- 480 [12] W. Dai, G. Wu, L. Li, N. Guan, M. Hunger, Mechanism of the
481 deactivation of SAPO-34 materials with different crystal sizes applied as
482 MTO catalysts. ACS Catal. 3 (2013) 588-596.
- 483 [13] D. Chen, K. Moljord, T. Fuglerud, A. Holmen, The effect of crystal size of
484 SAPO-34 on the selectivity and deactivation of the MTO reaction.
485 Micropor. Mesopor. Mater. 29 (1999) 191-203.
- 486 [14] Y. Hirota, K. Murata, M. Miyamoto, Y. Egashira, N. Nishiyama, Light
487 olefins synthesis from methanol and dimethyl ether over SAPO-34
488 nanocrystals. Catal. Lett. 140 (2010) 22-26.

- 489 [15] M. Firoozi, M. Baghalha, M. Asadi, The effect of micro and nano particle
490 size of H-ZSM-5 on the selectivity of MTP reaction. *Catal. Comm.* 10
491 (2009) 1582-1585.
- 492 [16] H. Konno, T. Okumara, T. Kawahara, Y. Nakasaka, T. Tago, T. Masuda,
493 Kinetics of n-hexane cracking over ZSM-5 zeolites-effect of crystal size
494 on effectiveness factor and catalyst lifetime. *Chem. Eng. J.* 207 (2012)
495 490-496.
- 496 [17] M. V. Landau, L. Vradman, V. Valtchev, J. Lezervant, E. Liubich, M.
497 Talianker, Hydrocracking of heavy vacuum gas oil with Pt/H-beta-Al₂O₃
498 catalyst: effect of zeolite crystal size in the nanoscale range. *Ind. Eng.*
499 *Chem. Res.* 42 (2003) 2773-2782.
- 500 [18] M. A. Cambor, A. Corma, A. Martínez, V. Martínez-Soria, S. Valencia,
501 Mild hydrocracking of vacuum gasoil over NiMo-Beta zeolite catalysts:
502 the role of the location of the NiMo phases and the crystallite size of the
503 zeolite. *J. Catal.* 179 (1998) 537-547.
- 504 [19] A. Martínez, C. López, The influence of ZSM-5 zeolite composition and
505 crystal size on the in situ conversion of Fischer-Tropsch products over
506 hybrid catalysts. *Appl. Catal. A* 294 (2005) 251-259.
- 507 [20] Y. Lee, M.B. Park, P.S. Kim, A. Vicente, C. Fernandez, I.-S. Nam, S.B.
508 Hong, Synthesis and catalytic behavior of ferrierite nanoneedles. *ACS*
509 *Catal.* 3 (2013) 617-621.

- 510 [21] P. Ratnasamy, G.P. Babu, A. J. Chandwadkar, S. B. Kilkarmi, Influence of
511 crystal size of HZSM-5 on activity and shape selectivity in xylene
512 isomerization. *Zeolites* 6 (1986) 98-100.
- 513 [22] A. Zheng, Z. Zhao, S. Chang, Z. Huang, H. Wu, X. Wang, F. He, H. Li,
514 Effect of crystal size of ZSM-5 on the aromatic yield and selectivity from
515 catalytic fast pyrolysis of biomass. *J. Mol. Catal. A: Chem.* 383 (2014)
516 23-30.
- 517 [23] T. Meng, D. Mao, Q. Guo, G. Lu, The effect of crystal sizes of HZSM-5
518 zeolites in ethanol conversion to propylene. *Catal. Commun.* 21 (2012) 52-
519 57.
- 520 [24] C. Herrmann, J. Haas, F. Fetting, Effect of the crystal size on the activity
521 of ZSM-5 crystals catalysts in various reactions. *Appl. Catal.* 35 (1987)
522 299-310.
- 523 [25] S. Mintova, J.-P. Gilson, V. Valtchev, Advance in nanosized zeolites.
524 *Nanoscale* 5 (2013) 6693-6703.
- 525 [26] J. Grand, H. Awala, S. Mintova, Mechanism of zeolites crystal growth:
526 new findings and open questions. *Cryst. Eng. Comm.* 18 (2016) 650-664.
- 527 [27] F. Di Renzo, Zeolites as tailor-made catalysts: control of the crystal size.
528 *Catal. Today* 41 (1998) 37-40.
- 529 [28] V. Valtchev, S. Mintova, V. Dimov, A. Toneva, D. Radev, Tribochemical
530 activation of seeds for rapid crystallization of zeolite Y. *Zeolites* 15 (1995)
531 193-197.

- 532 [29] X. Chen, T. Todorova, A. Vimont, V. Ruaux, Z. Qin, J.-P. Gilson, V.
533 Valtchev, In situ and post-synthesis control of physicochemical properties
534 of FER-type crystals. *Micropor. Mesopor. Mater.* 200 (2014) 334-342.
- 535 [30] Y. Kamimura, K. Itabashi, T. Okubo, Seed-assisted, OSDA-free synthesis
536 of MTW-type zeolite and “Green MTW” from sodium aluminosilicates gel
537 systems. *Micropor. Mesopor. Mater.* 147 (2012) 149-156.
- 538 [31] Q. Li, B. Mihailova, D. Creaser, J. Sterte, Aging effects on the nucleation
539 and crystallization kinetics of colloidal TPA-silicalite-1. *Micropor.*
540 *Mesopor. Mater.* 43 (2001) 51-59.
- 541 [32] X. Zhang, D. Tang, G. Jiang, Synthesis of zeolite NaA at room
542 temperature: the effect of synthesis parameters on crystal size and its size
543 distribution. *Adv. Powder Technol.* 24 (2013) 689-696.
- 544 [33] K. Iwakai, T. Tago, H. Konno, Y. Nakasaka, T. Masuda, Preparation of
545 nano-crystalline MFI zeolite via hydrothermal synthesis in
546 water/surfactant/organic solvent using fumed silica as Si source.
547 *Micropor. Mesopor. Mater.* 141 (2011) 167-174.
- 548 [34] T. Tago, D. Aoki, K. Iwakai, T. Masuda, Preparation for size-controlled
549 MOR zeolite nanocrystal using water/surfactant/organic solvent. *Top.*
550 *Catal* 52 (2009) 865-871.
- 551 [35] N.L. Chauhan, J. Das, R.V. Jasra, Z.V.P. Murthy, P.A. Parikh, Synthesis
552 of zeolite ZSM-5: effect of emulsifiers. *Cryst. Res. Technol.* 47 (2012)
553 746-753.

- 554 [36] N.L. Chauhan, Z.V.P. Murthy, J. Das, P.A. Parikh, Synthesis of zeolite
555 ferrierite-Role of emulsifiers. *Indian J. Chem. Technol.* 18 (2011) 335-
556 342.
- 557 [37] E. Catizzone, A. Aloise, M. Migliori, G. Giordano, Dimethyl ether
558 synthesis via methanol dehydration: effect of zeolite structure. *Appl. Catal.*
559 A 502 (2015) 215-220.
- 560 [38] E. Catizzone, A. Aloise, M. Migliori, G. Giordano, , From 1-D to 3-D
561 zeolite structures: performances assessment in catalysis of vapour-phase
562 methanol dehydration to DME. *Micropor. Mesopor. Mater.* 243 (2017)
563 102-111.
- 564 [39] E. Catizzone, M. Migliori, A. Purita, G. Giordano, Ferrierite vs. γ -Al₂O₃:
565 the superiority of zeolites in terms of water-resistance in vapour-phase
566 dehydration of methanol to dimethyl ether. *J. Energ. Chem*, 2018, DOI:
567 10.1016/j.jechem.2018.05.004
- 568 [40] G. Bonura, F. Frusteri, C. Cannilla, G. Drago Ferrante, A. Aloise, E.
569 Catizzone, M. Migliori, G. Giordano, Catalytic features of CuZnZr-zeolite
570 hybrid systems for the direct CO₂-to-DME hydrogenation reaction. *Catal.*
571 *Today* 277 (2016) 48-54.
- 572 [41] F. Frusteri, M. Migliori, C. Cannilla, L. Frusteri, E. Catizzone, A. Aloise,
573 G. Giordano, G. Bonura, Direct CO₂-to-DME hydrogenation reaction:
574 new evidences of a superior behaviour of FER-based hybrid systems to
575 obtain high DME yield. *J. CO₂ Util.* 18 (2017) 353-361.

- 576 [42] G. Bonura, M. Migliori, L. Frusteri, C. Cannilla, E. Catizzone, G.
577 Giordano, F. Frusteri, Acidity control of zeolite functionality on activity
578 and stability of hybrid catalysts during DME production via CO₂
579 hydrogenation. *J. CO₂ Util.* 24 (2018) 398-406.
- 580 [43] E. Catizzone, G. Bonura, M. Migliori, F. Frusteri, G. Giordano, CO₂
581 recycling to dimethyl ether: state-of-the-art and perspectives. *Molecules*,
582 23 (2018) 31-58.
- 583 [44] G. Centi, S. Perathoner, Opportunities and prospects in the chemical
584 recycling of carbon dioxide to fuels. *Catal. Today* 148 (2009) 191-205.
- 585 [45] Z. Azizi, M. Rezaeimanesh, T. Tohidian, M. R. Rahimpour, Dimethyl
586 ether: a review of technologies and production challenges. *Chem. Eng.*
587 *Process.* 82 (2014) 150-172.
- 588 [46] E. Catizzone, A. Aloise, M. Migliori, G. Giordano, The effect of FER
589 zeolite acid sites in methanol-to-dimethyl ether catalytic dehydration. *J.*
590 *Energ. Chem.* 26 (2017) 406-415.
- 591 [47] A.A. Rownaghi, F. Rezaei, M. Stante, J. Hedlund, Selective dehydration of
592 methanol to dimethyl ether on ZSM-5 nanocrystals. *Appl. Catal. B: Env.*
593 119 (2012) 56-61.
- 594 [48] A. Aloise, E. Catizzone, M. Migliori, J. B. Nagy, G. Giordano, Catalytic
595 behaviour in propane aromatization using Ga-MFI catalyst. *Chin. J. Chem.*
596 *Eng.* 25 (2017) 1863-1870.

- 597 [49] M. Migliori, A. Aloise, E. Catizzone, G. Giordano, Kinetic analysis of
598 methanol to dimethyl ether reaction over H-MFI catalyst. *Ind. Eng. Chem.*
599 *Res.* 53 (2014) 14885-14891.
- 600 [50] A. Bonilla, D. Baudouin, J. Perez-Ramírez, Desilication of ferrierite
601 zeolite for porosity generation and improved effectiveness in polyethylene
602 pyrolysis. *J. Catal.* 265 (2009) 170-180.
- 603 [51] A. A. Rownaghi, F. Rezaei, J. Hedlund, Uniform mesoporous ZSM-5
604 single crystals catalyst with high resistance to coke formation for
605 methanol deoxygenation. *Microp. Mesop. Mater.* 151 (2012) 26-33.
- 606 [52] G. Leofanti, M. Padovan, G. Tozzola, B. Venturelli, Surface area and pore
607 texture of catalysts. *Catal. Today.* 4 (1998) 207-219.
- 608 [53] A. A. Rownaghi, J. Hedlund, Methanol to gasoline-range hydrocarbons:
609 influence of nanocrystal size and mesoporosity on catalytic performances
610 and product distribution of ZSM-5. *Ind. Eng. Chem. Res.* 50 (2010)
611 11872-11878.
- 612 [54] A. A. Rownaghi, F. Rezaei, J. Hedlund, Yield of gasoline-range
613 hydrocarbons as a function of uniform ZSM-5 crystal size. *Catal. Comm.*
614 14 (2011) 37-41.
- 615 [55] M. Trombetta, T. Armaroli, A.G. Alejandre, J.R. Solis, G. Busca, An FT-
616 IR study of the internal and external surfaces of HZSM5 zeolite. *Appl.*
617 *Catal. A: Gen.* 192 (2000) 125-136.

- 618 [56] Y.P. Khitev, Y.G. Kolyagin, I.I. Ivanova, O.A. Ponomareva, F. Thibault-
619 Starzyk, J.-P. Gilson, C. Fernandez, F. Fajula, Synthesis and catalytic
620 properties of hierarchical micro/mesoporous materials based on FER
621 zeolite. *Micropor. Mesopor. Mater.* 146 (2011) 201-207.
- 622 [57] J. Datka, M. Kawalek, K. Góra-Marek, Acid properties of NaKH-
623 ferrierites of various exchange degrees studied by IR spectroscopy. *Appl.*
624 *Catal. A: Gen.* 243 (2003) 293-299.
- 625 [58] P. Cañozares, A. Carrero, P. Sánchez, Isomerization of n-butene over
626 ferrierite zeolite modified by silicon tetrachloride treatment. *Appl. Catal.*
627 *A: Gen.* 190 (2000) 93-105
- 628 [59] D.P.B. Peixoto, S.M. Cabral de Menezes, M.I. Pais da Silva, Influence of
629 different processes of dealumination on acid properties of an H-ferrierite
630 zeolite. *Mater. Lett.* 57 (2003) 3933-3942.
- 631 [60] B. Wichterlová, Z. Tvarůková, Z. Sobalík, P. Sarv, Determination and
632 properties of acid sites in H-ferrierite: a comparison of ferrierite and MFI
633 structures. *Micropor. Mesopor. Mat.* 24 (1998) 223 – 233.
- 634
635 [61] C. Pazé, A. Zecchina, S. Spera, G. Spano, F. Rivetti, Acetonitrile as probe
636 molecule for an integrated ¹H NMR and FTIR study of zeolitic Brønsted
637 acidity: interaction with zeolites H-ferrierite and H-beta. *Phys. Chem.*
638 *Chem. Phys.* 2 (2000) 5756-5760.
- 639
640 [62] S. van Donk, E. Bus, A. Broersma, J.H. Bitter, K.P. de Jong, Probing the
641 accessible sites for n-butene skeletal isomerization over aged and selective
642 H-ferrierite with d₃-acetonitrile. *J. Catal.* 212 (2002) 86-93.

- 643 [63] P.A. Jacobs, C.F. Heylen, Active sites in zeolites. *J. Catal.* 34 (1974) 267-
644 274.
- 645 [64] C. Morterra, G. Cerrato, G. Meligrana, Revisiting the use of 2,6-
646 dimethylpyridine adsorption as probe molecule for the acidic properties of
647 metal oxides. *Langmuir* 17 (2001) 7053-7060.
- 648 [65] F. Thibault-Starzyk, I. Stan, S. Abellò, A. Bonilla, K. Thomas, C.
649 Fernandez, J.-P. Gilson, J. Perez-Ramírez, Quantification of enhanced acid
650 site accessibility in hierarchical zeolites – the accessibility index. *J. Catal.*
651 264 (2009) 11-14.
- 652 [66] T. Onfroy, G. Clet, M. Houalla, Quantitative IR characterization of the
653 acidity of various oxide catalysts. *Micropor. Mesopor. Mater.* 82 (2005)
654 99-104.
- 655 [67] K. Sadowska, K. Góra-Marek, J. Datka, Accessibility of acid sites in
656 hierarchical zeolites: quantitative IR studies of pivalonitrile adsorption. *J.*
657 *Phys. Chem. C* 117 (2013) 9237-9244.
- 658 [68] T. Montanari, M. Bevilacqua, G. Busca, Use of nitrile as probe molecules
659 for the accessibility of the active sites and the detection of complex
660 interactions in zeolites through IR spectroscopy. *Appl. Catal. A: Gen.* 307
661 (2006) 21-29.
- 662 [69] M. Cai, A. Palčić, V. Subramanian, S. Moldovan, O. Ersen, V. Valtchev,
663 V.V. Ordonsky, A. Y. Khodakov, Direct dimethyl ether synthesis from

- 664 syngas on copper-zeolite hybrid catalysts with a wide range of zeolite
665 particle size. *J. Catal.* 338 (2016) 227-238.
- 666 [70] M. Boudart, Turnover rates in heterogeneous catalysis. *Chem Rev.* 95
667 (1995) 661-666.
- 668 [71] M. Bjørgen, S. Svelle, F. Joensen, J. Nerlov, S. Kolboe, F. Bonino, L.
669 Palumbo, S. Bordiga, U. Olsbye, Conversion of methanol to hydrocarbons
670 over zeolite H-ZSM-5: on the origin of the olefinic species. *J. Catal.* 249
671 (2007) 195-207.
- 672 [72] P. Tian, Y. Wei, M. Ye, Z. Liu, Methanol to olefins (MTO): from
673 fundamentals to commercialization. *ACS Catal.* 5 (2015) 1922-1938.
- 674 [73] J.F. Haw, W. Song, D.M. Marcus, J.B. Nicholas, The mechanism of
675 methanol to hydrocarbon catalysis. *Acc. Chem. Res.* 36 (2003) 317-326.
- 676 [74] M. Stöcker, Methanol-to-hydrocarbons: catalytic materials and their
677 behavior. *Micropor. Mesopor. Mater.* 29 (1999) 3-48.
- 678 [75] K.P. Möller, W. Böhringer, A.E. Schnitzler, E. van Steen, C.T. O'Connor,
679 The use of a jet loop reactor to study the effect of crystal size and the co-
680 feeding of olefins and water on the conversion of methanol over ZSM-5.
681 *Micropor. Mesopor. Mater.* 29 (1999) 127-144.
- 682 [76] M. Guisnet, P. Magnoux, Organic chemistry of coke formation. *Appl.*
683 *Catal. A: Gen.* 212 (2001) 83-96.
- 684 [77] U. Olsbye, S. Svelle, M. Bjørgen, P. Beato, T.V.W. Janssens, F. Joensen,
685 S. Bordiga, K.P. Lillerud, Conversion of methanol to hydrocarbons: how

686 zeolite cavity and pore size controls product selectivity. *Angew. Chem.* 51
687 (2012) 5810–5831.

688 [78] X.-J. Liu, Y.-D. Zhang, L. Sun, W.-Q. Deng, Computational screening of
689 zeolite catalysts for MTO reaction. *Chemistry Select.* 2 (2017) 10290-
690 10294.

691

692

693

694

695

696

697 **TABLES CAPTIONS**

698 **Table 1** - Physicochemical characteristics of the series of studied zeolite samples.

699 **Table 2** - Acidic properties of the series of studied samples.

700 **Table 3** – Apparent turnover frequency at 180 °C, DME selectivity at 240°C and 280

701 °C, and by-products distribution at 280 °C

702 **Table 4** - Coke formation: kinetic parameters for 1st order model.

703

704

705 **FIGURES CAPTIONS**

706 **Figure 1** – XRD patterns of studied samples.

707 **Figure 2** – SEM images of studied samples.

708 **Figure 3** – Nitrogen adsorption/desorption isotherms of studied samples.

709 **Figure 4** – FT-IR spectra of studied samples after evacuation at 723 K for 4h (A) and
710 after adsorption of D₃-acetonitrile at room temperature (B).

711 **Figure 5** – Difference FT-IR spectra of studied samples after saturation with 2,6-
712 dimethyl pyridine (A) or tert-butyl nitrile (B).

713 **Figure 6**– Methanol conversion as a function of reaction temperature.

714 **Figure 7**– Coke content in zeolite catalysts deposited at 240°C as a function of TOS. .

715 **Figure 8** – GC-MS spectra of carbonaceous deposit extracted from soluble coke of
716 studied samples after 5 h, 15 h and 60 h reaction at 240 °C.

717 **Figure 9** – DTA profiles of studied samples after 5 h, 15 h and 60 h reaction at 240 °C.

718 **Figure 10** – HTC/LTC ratio as a function of reaction time.

719 **Figure 11** –EDX mapping images of studied samples after 60 h reaction at 240 °C.

720

Sample	Average crystal size (μm)	Al/(Si+Al)		AS/AC ratio	$\text{Al}_{\text{EF}}^{\text{c}}$ (%)	$\text{S}_{\text{BET}}^{\text{d}}$ (m^2/g)	$\text{V}_{\text{mic}}^{\text{e}}$ (m^2/g)
		(mol%)					
		In crystal (AC) ^a	On surface (AS) ^b				
M-FER	5-10	9.6	11.4	1.2	14	332	0.134
NP-FER	0.3-0.5	10.4	13.0	1.3	17	314	0.125
NC-FER	0.1	9.4	13.3	1.4	21	304	0.122

^a Determined by AA

^b Determined by EDX

^c Percentage of aluminium in octahedral coordination estimated via ^{27}Al -NMR

^d BET surface area

^e Micropore volume calculated by t-plot method

Table 1

SAMPLE	Total acidity ^a		External acidity	
	(μmol/g)		(μmol/g)	
	Brønsted	Lewis	2,6-DMP ^b	TBN ^c
M-FER	598	489	15	12
NP-FER	363	948	12	13
NC-FER	276	521	8	10

^a Determined by FT-IR after adsorption of d₃-acetonitrile;

^b Determined by FT-IR after adsorption of 2,6-dimethyl pyridine;

^c Determined by FT-IR after adsorption of tert-butylnitrile.

Table 2

<i>SAMPLE</i>	<i>TOF_{app} at 180 °C</i> (<i>h⁻¹</i>)	<i>DME Selectivity</i>		<i>By-products loop distribution at 280 °C</i>		
		(%)		(%)		
		<i>240 °C</i>	<i>280 °C</i>	<i>Methane</i>	<i>Ethene</i>	<i>Propene</i>
<i>M-FER</i>	49	96	90	0.35	0.16	0.49
<i>NP-FER</i>	62	98	95	0.46	0.18	0.36
<i>NC-FER</i>	86	100	99	<i>N.D.</i>	<i>N.D.</i>	<i>N.D.</i>

Table 3

SAMPLE	C_{∞} (mg_{coke}/g_{cat})	τ (h)	r_0 (mg_{coke}/g_{cat}·h)	r^2 (-)
M-FER	73.9 ± 0.9	2.9 ± 0.2	25.5 ± 0.5	0.999
NP-FER	65.8 ± 0.4	5.1 ± 1.2	12.9 ± 2.0	0.983
NC-FER	45.3 ± 0.3	6.1 ± 0.1	7.4 ± 0.1	0.999

Table 4

Table 5

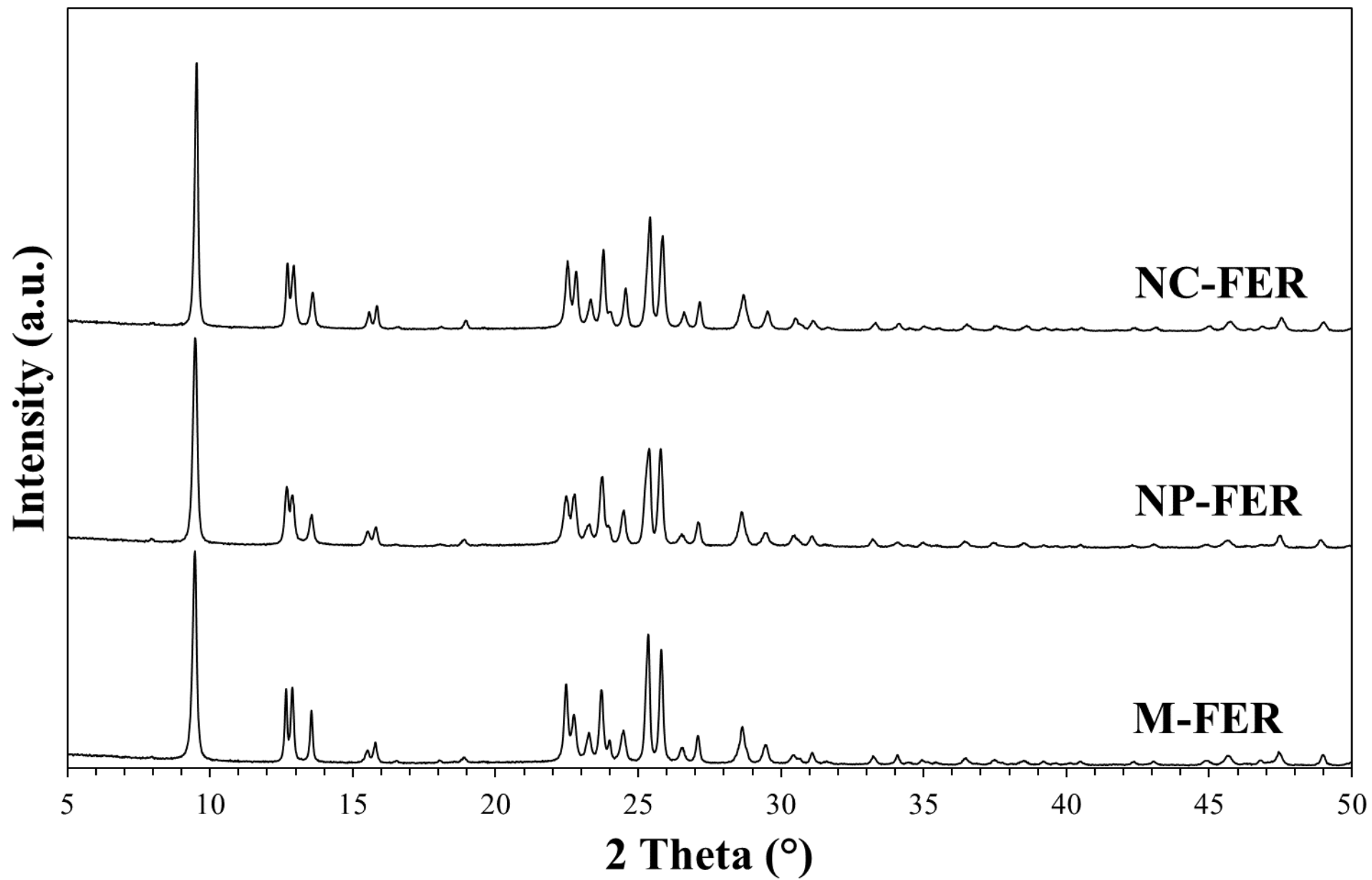


Figure 1

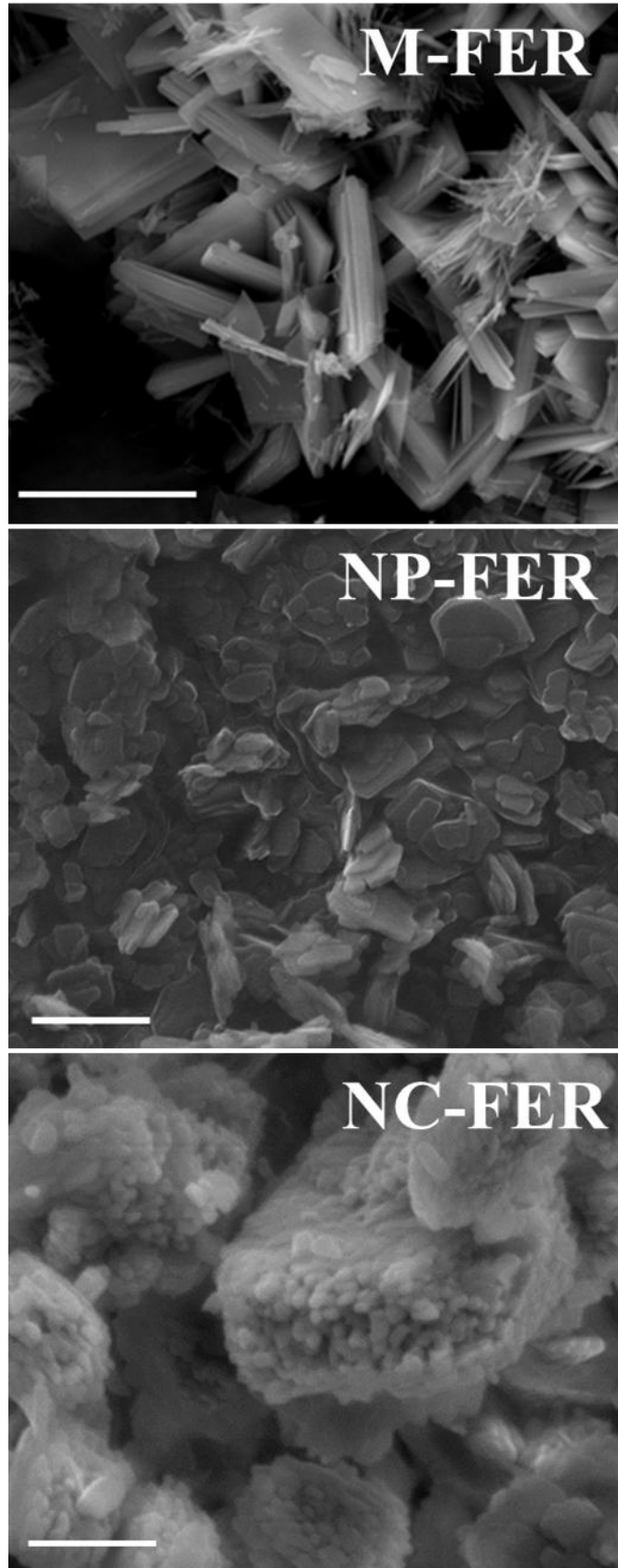


Figure 2

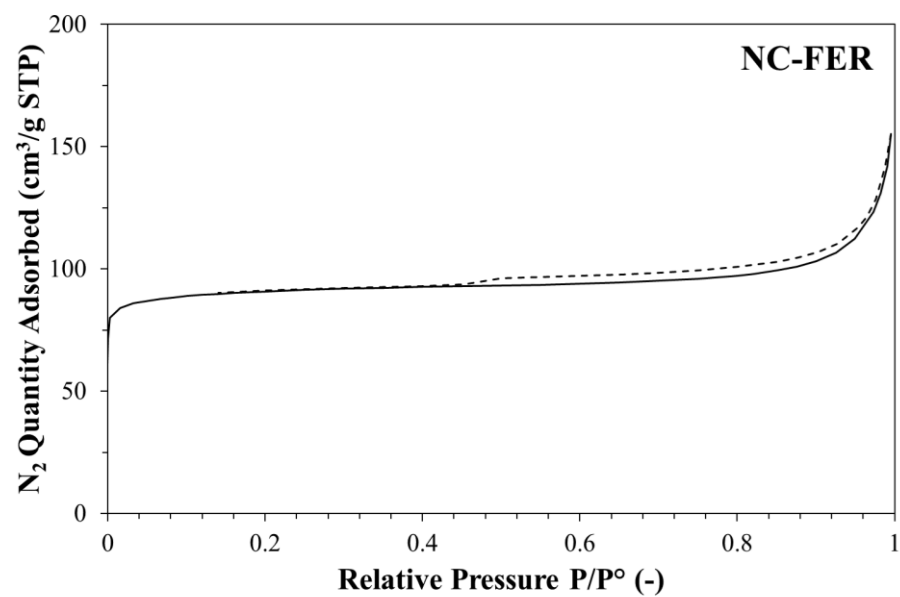
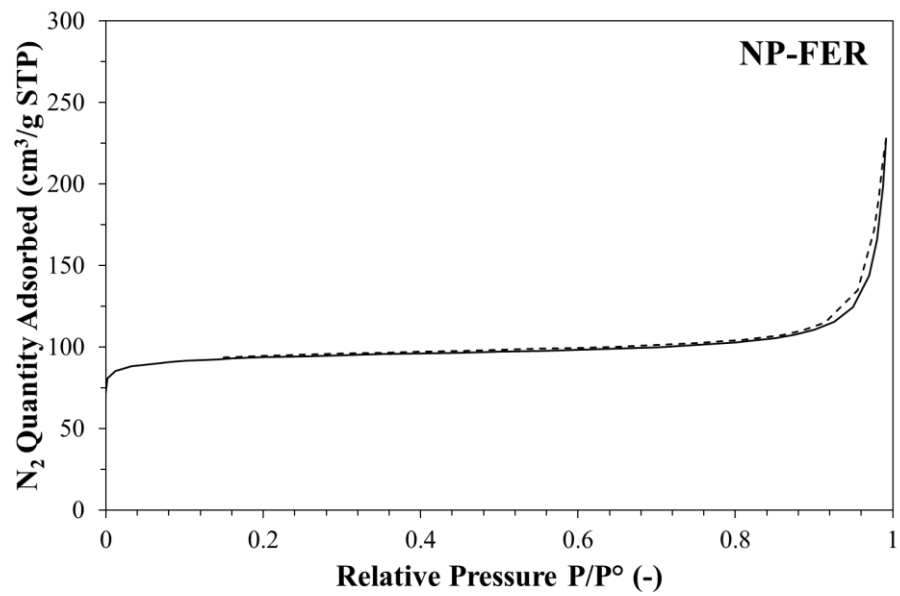
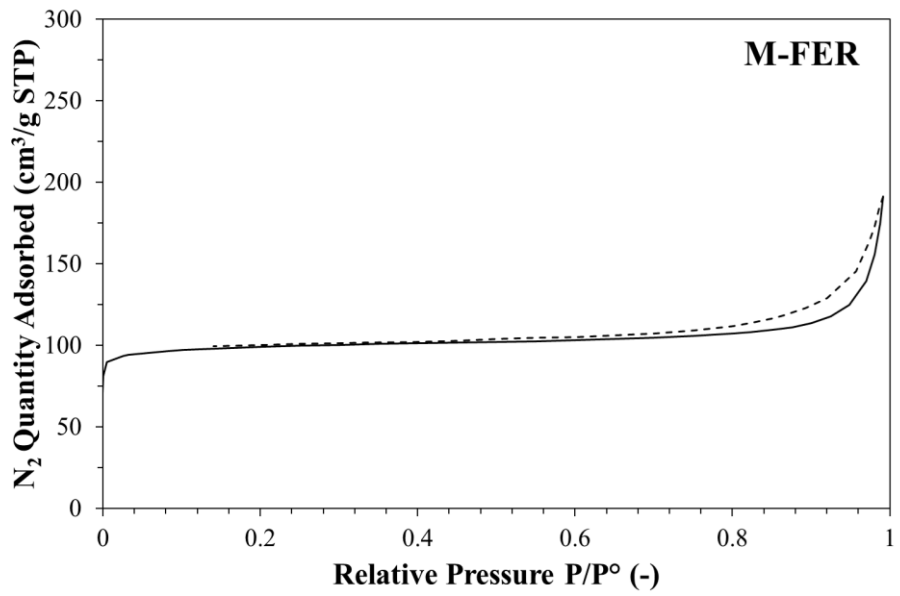


Figure 3

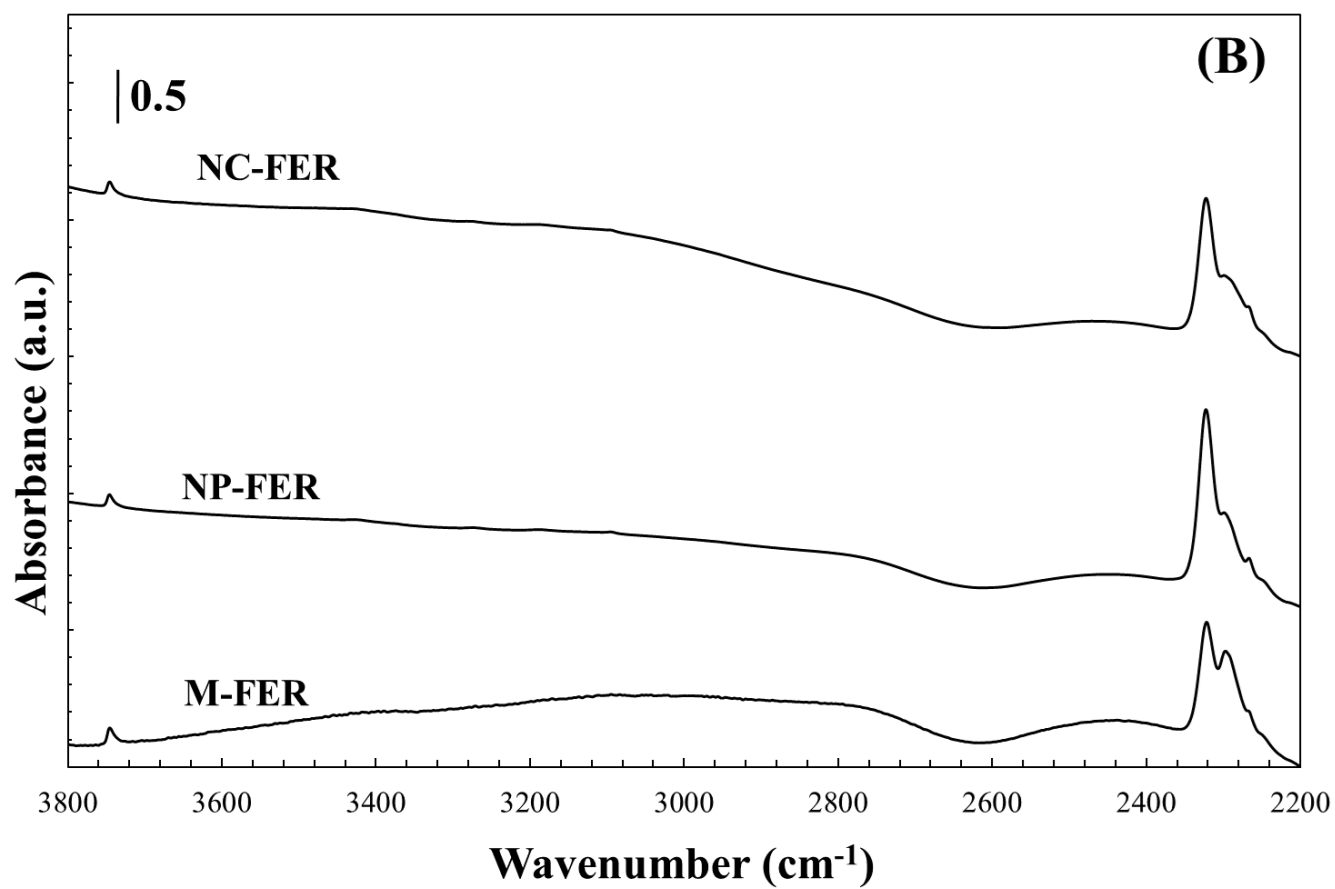
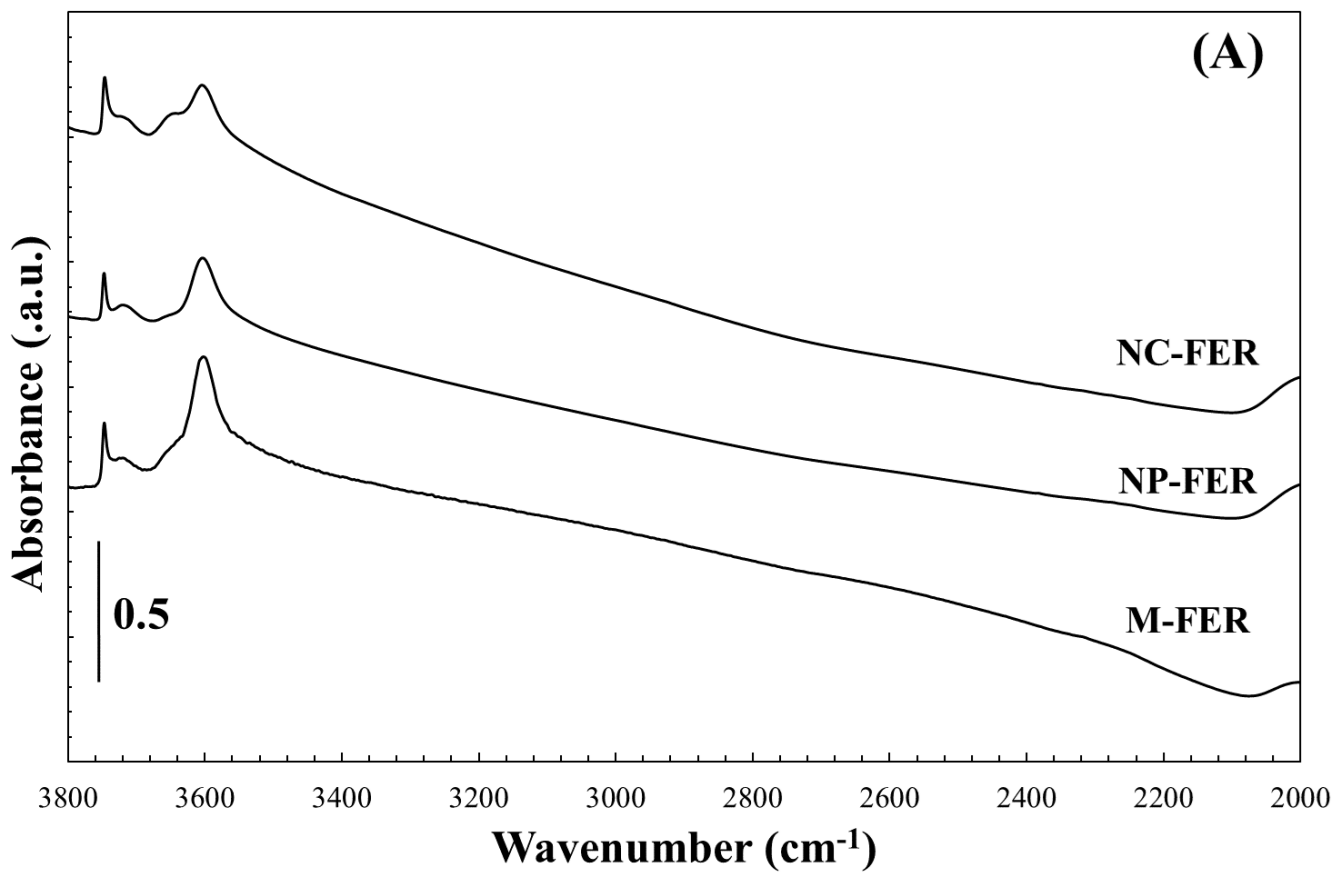


Figure 4

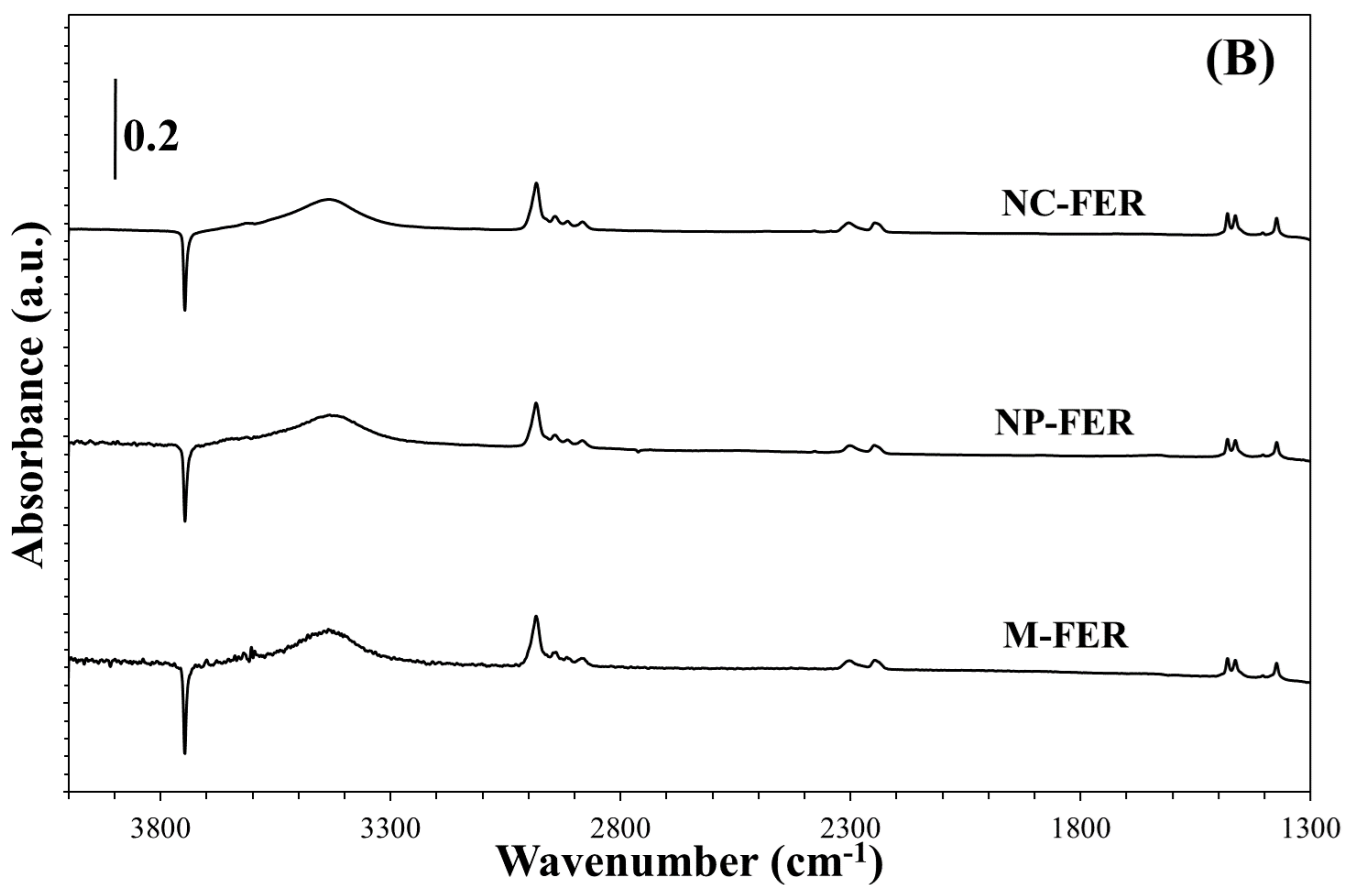
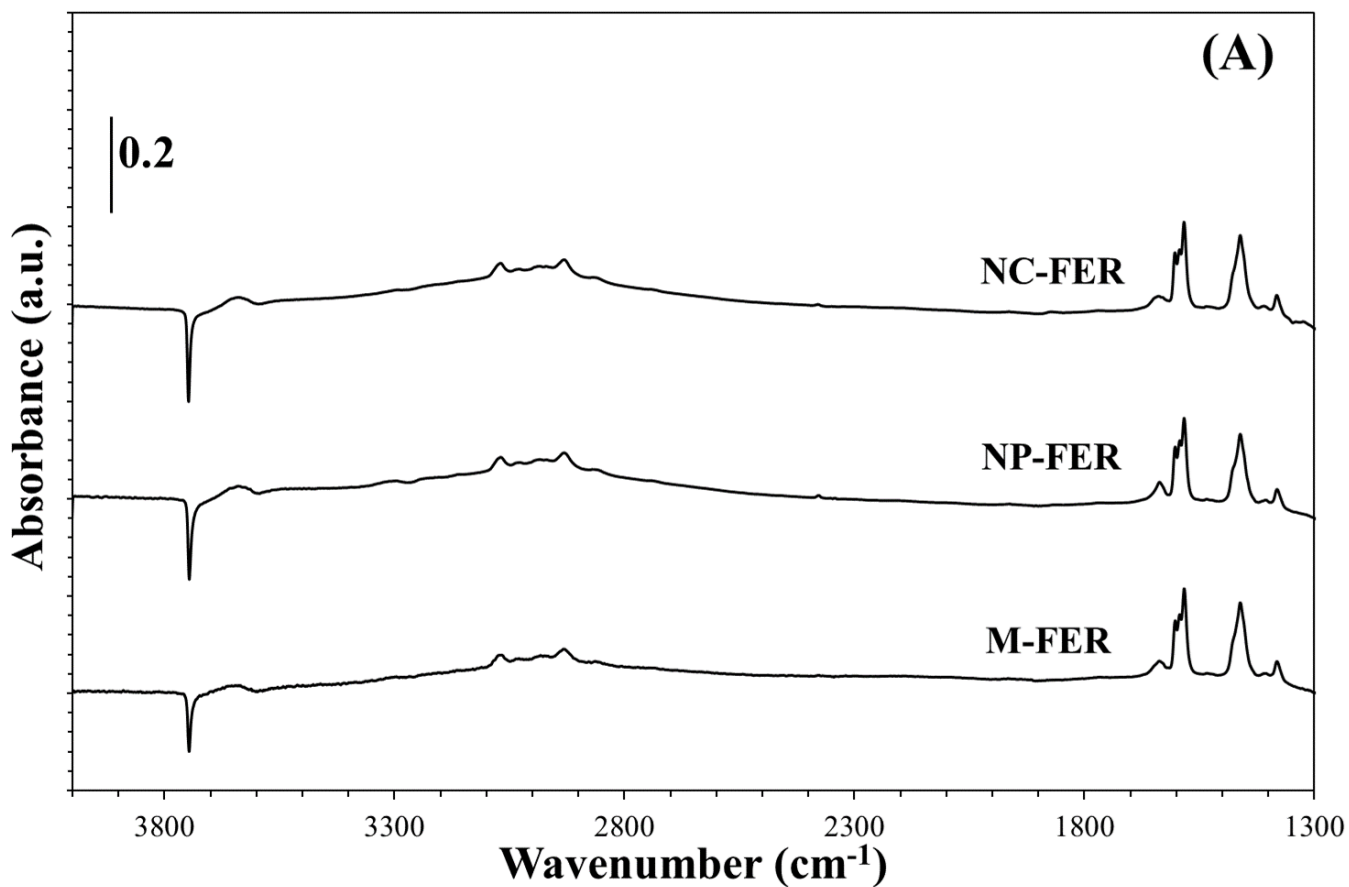


Figure 5

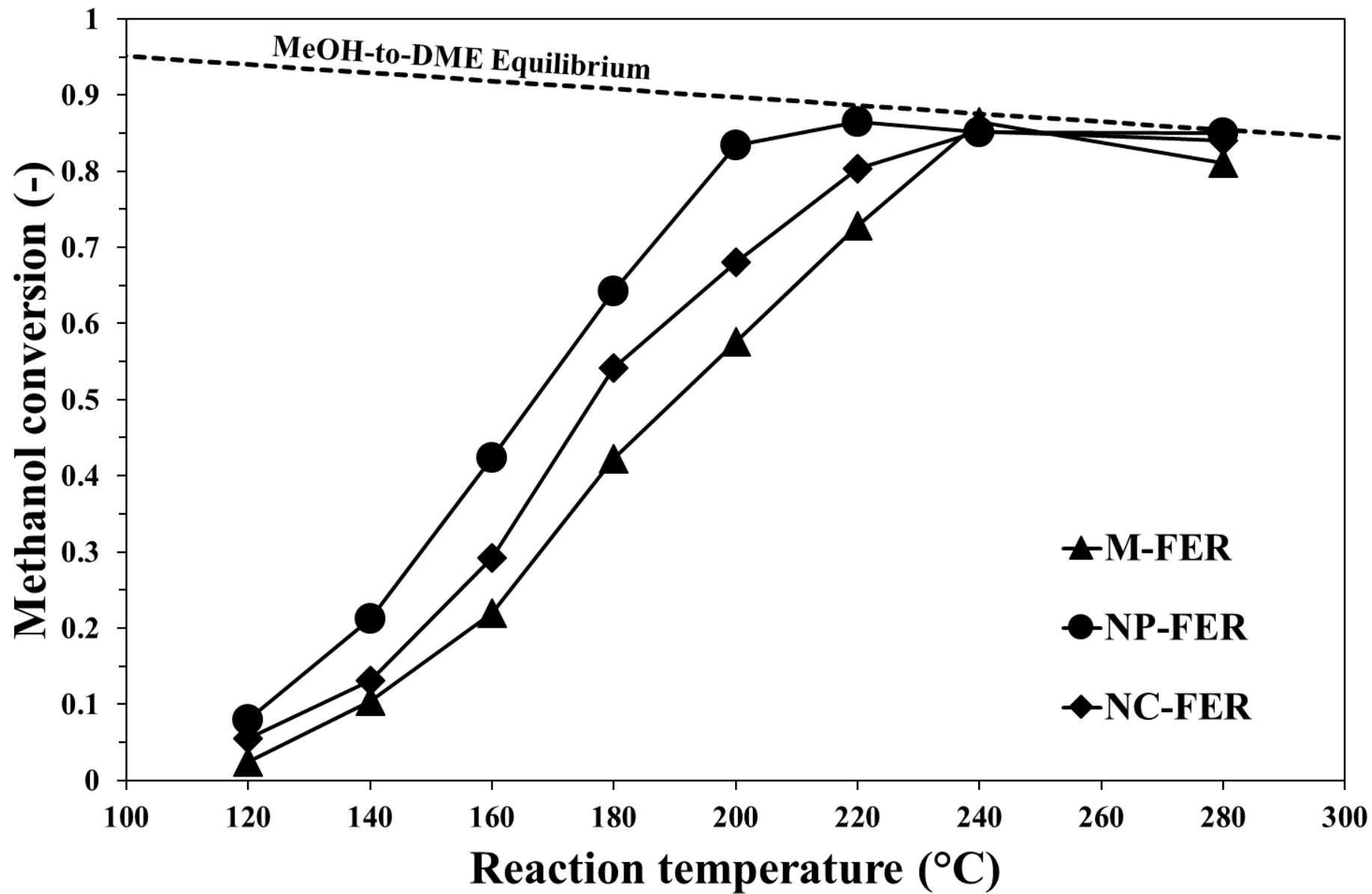


Figure 6

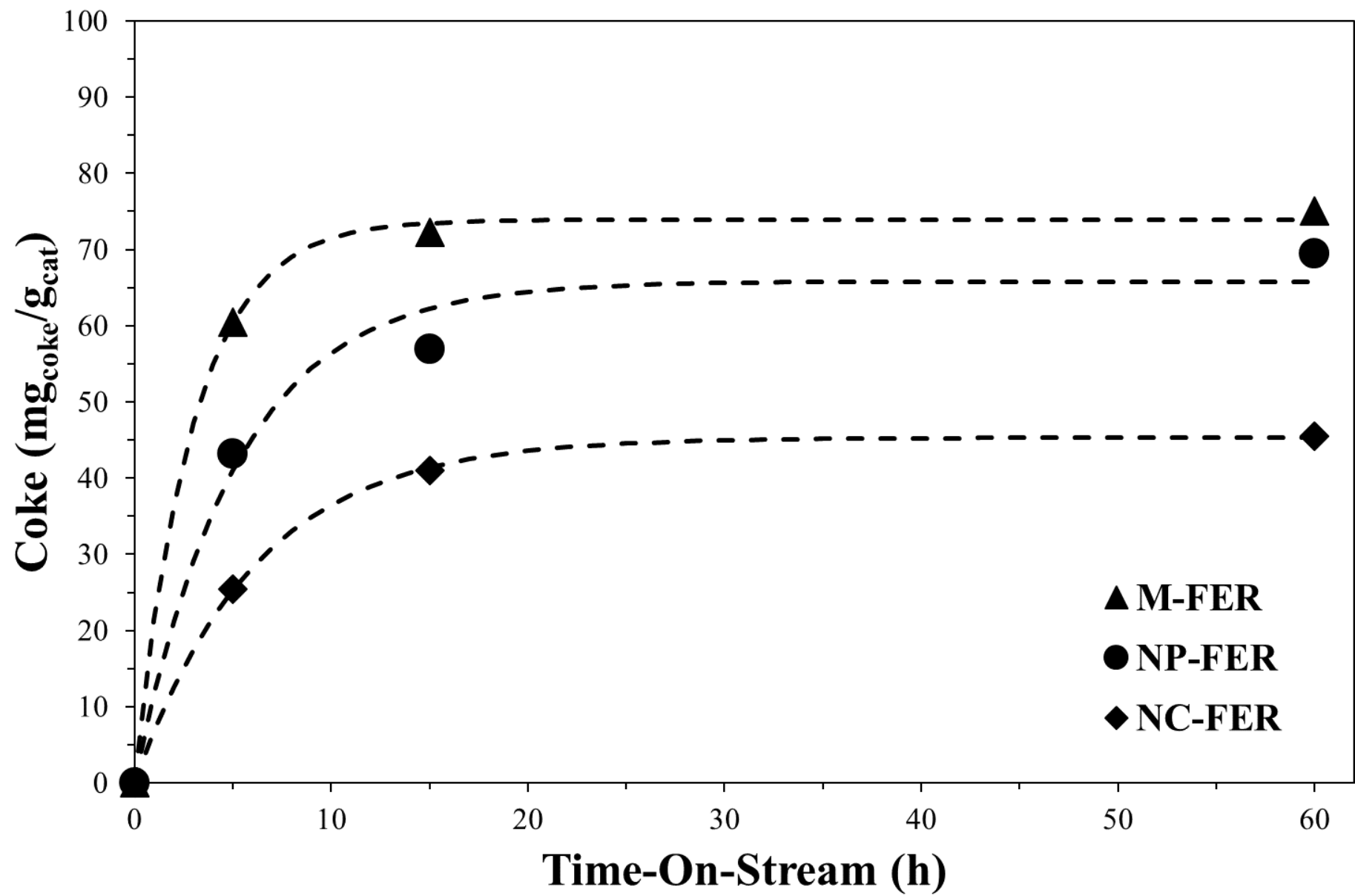


Figure 7

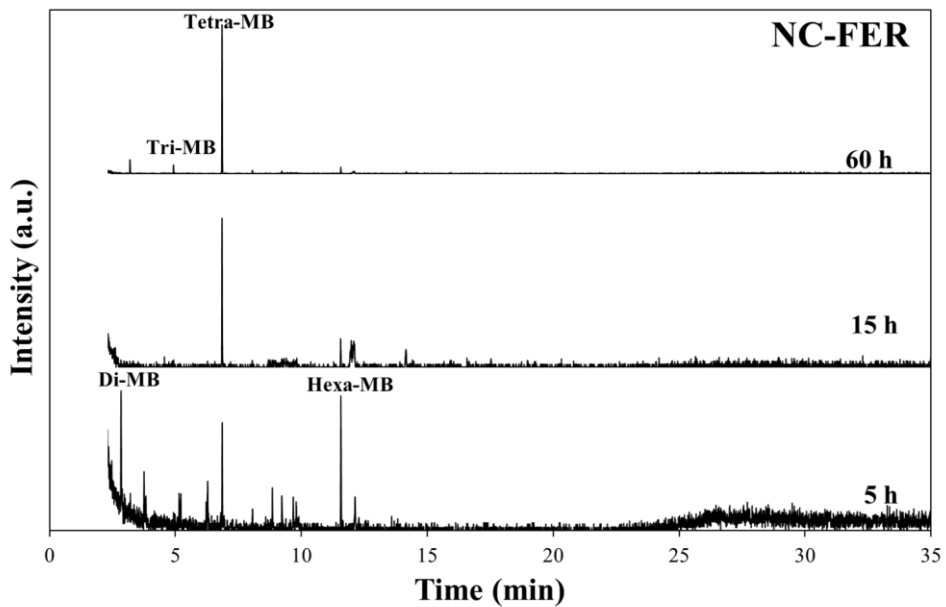
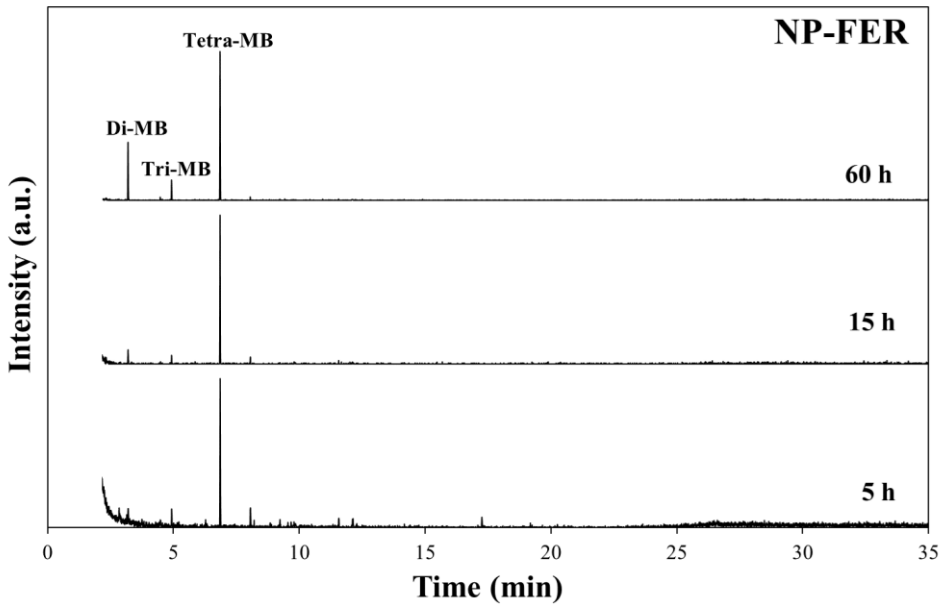
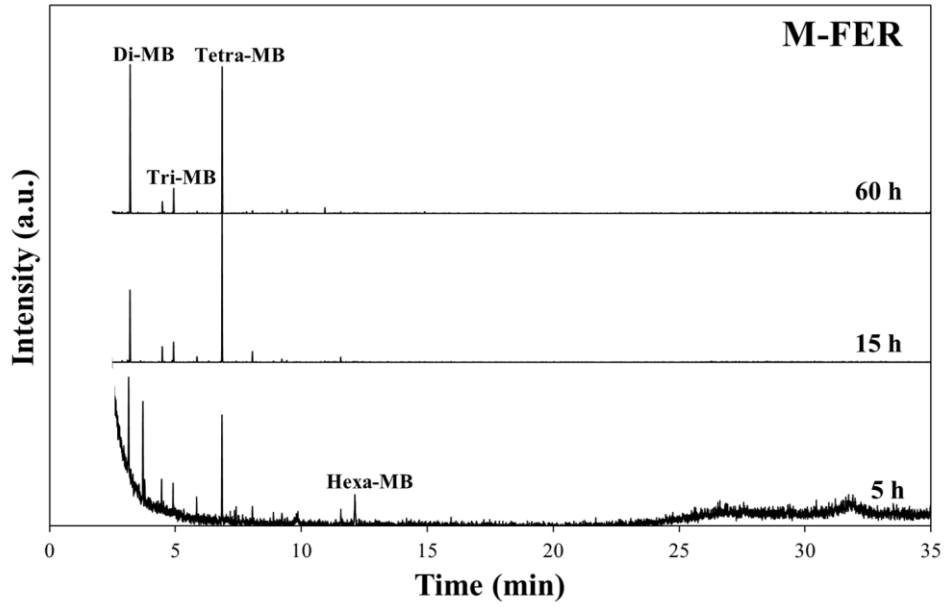


Figure 8

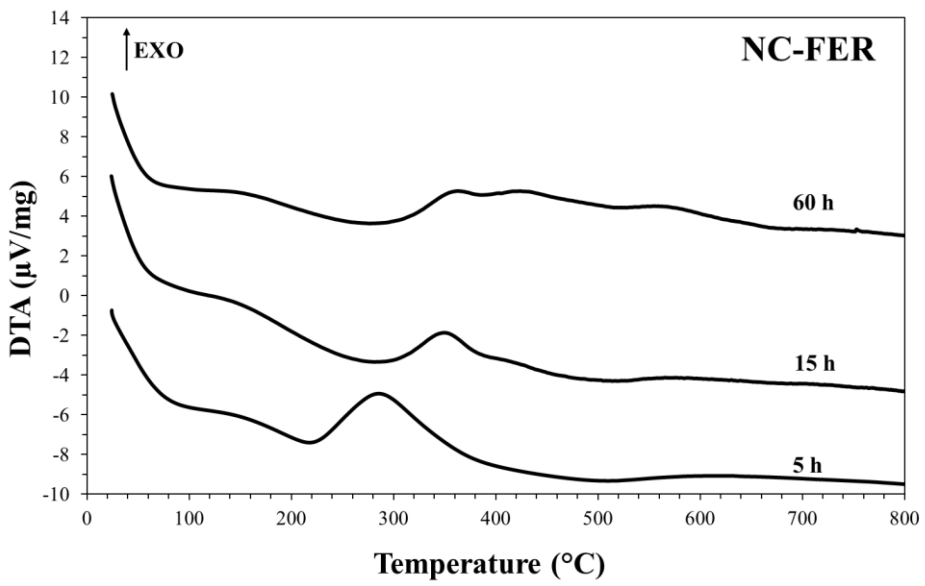
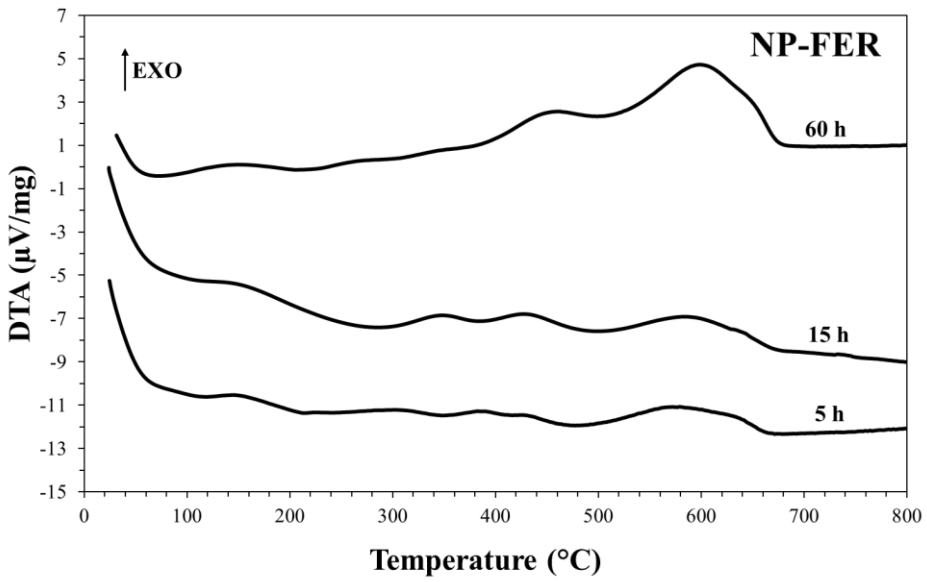
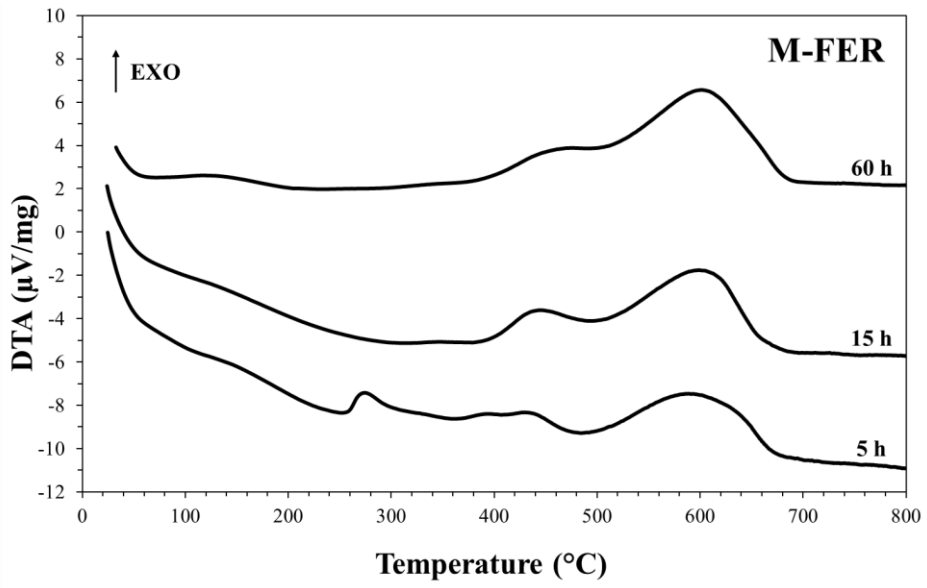


Figure 9

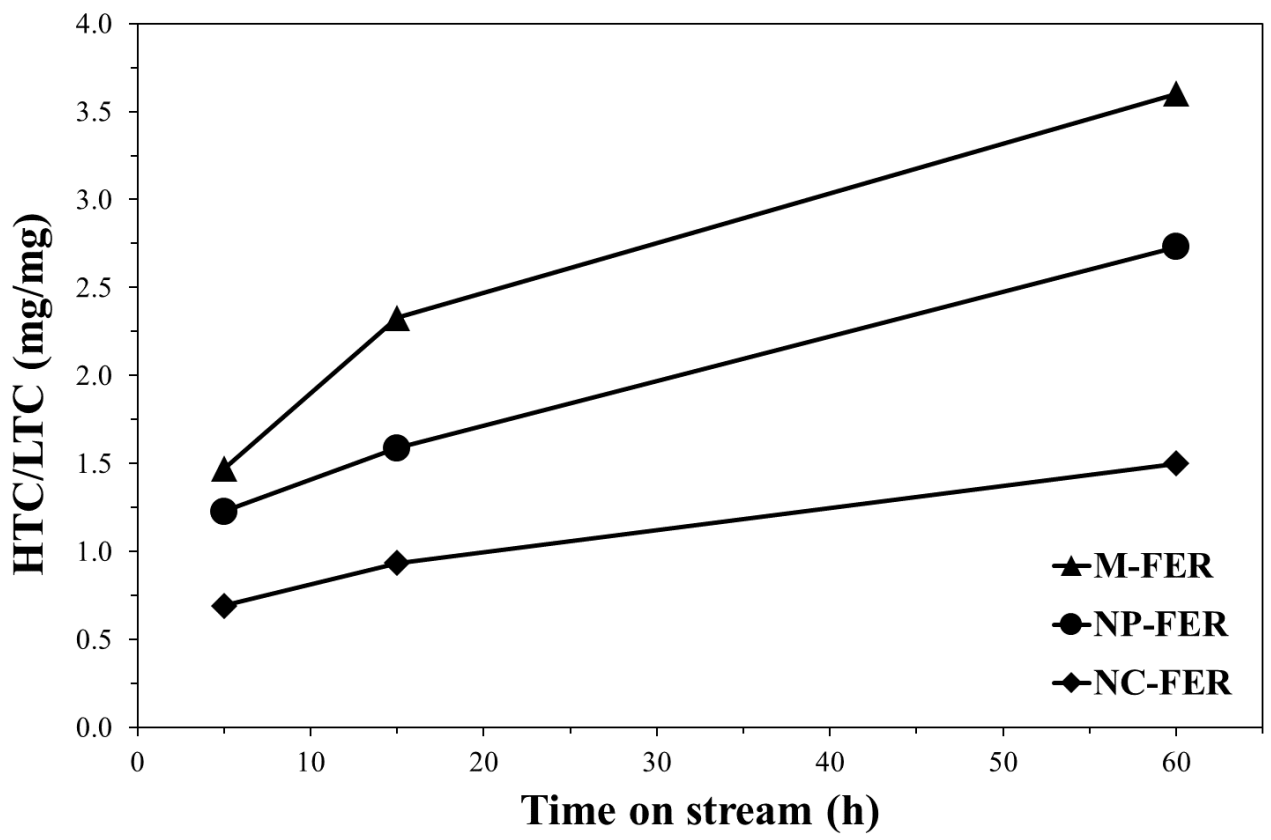


Figure 10

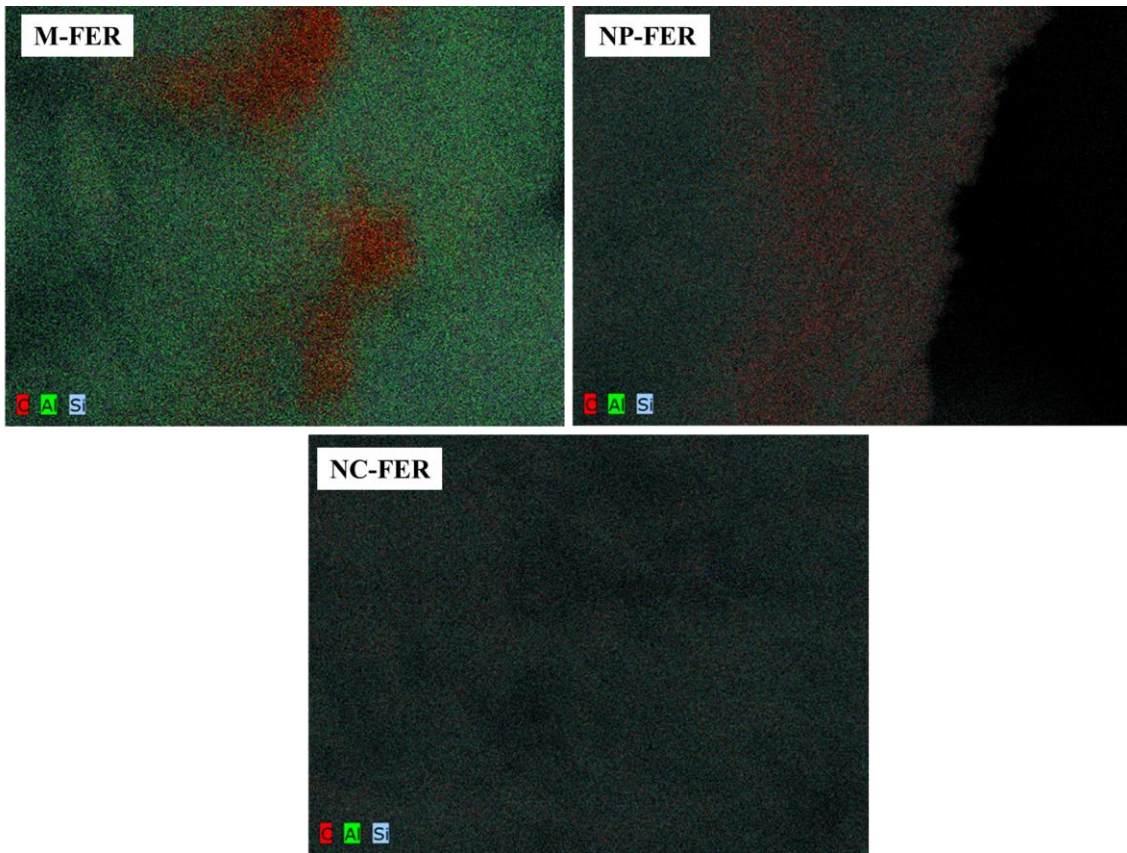


Figure 11